frontiers in Earth Science

ORIGINAL RESEARCH
published: 07 December 2021
doi: 10.3389/feart.2021.712443

Reconstructing 1200 years of Hydroclimate Variability in the Southern Margins of the Arabian Desert: Insights From a Paleo-Lake in Southern Yemen

Shah Parth[1]*, *James Russell*[2] and *Nicolas Waldmann*[1]

[1]Dr. Moses Strauss Department of Marine Geosciences, Charney School of Marine Sciences, University of Haifa, Haifa, Israel, [2]Department of Earth, Environmental and Planetary Sciences, Brown University, Providence, RI, United States

OPEN ACCESS

Edited by:
Davide Tiranti,
Agenzia Regionale per la Protezione Ambientale (ARPA), Italy

Reviewed by:
Priyeshu Srivastava,
University of São Paulo, Brazil
Steven L. Forman,
Baylor University, United States

***Correspondence:**
Shah Parth
pds.shah121@gmail.com

Specialty section:
This article was submitted to Quaternary Science, Geomorphology and Paleoenvironment, a section of the journal Frontiers in Earth Science

Received: *20 May 2021*
Accepted: *19 November 2021*
Published: *07 December 2021*

Citation:
Parth S, Russell J and Waldmann N (2021) Reconstructing 1200 years of Hydroclimate Variability in the Southern Margins of the Arabian Desert: Insights From a Paleo-Lake in Southern Yemen. Front. Earth Sci. 9:712443. doi: 10.3389/feart.2021.712443

The climate of the Arabian Desert is not well documented during the past two millennia due to the scarcity of continuous and well-dated terrestrial archives in the region. Reliable interpretation from the climatic records from this region are pivotal for identifying periodicities of inter-annual to multi-decadal variability and trends driven by shifts in position of the Intertropical Convergence Zone (ITCZ) and the strength of the monsoons. A high-resolution multiproxy approach is presented for a ~3.3 m composite core, GBW, from a karst lake located in Ghayl ba Wazir, southern Yemen. Sedimentary proxies, including particle size distribution, coupled with magnetic susceptibility (MS) and geochemistry (XRF), provide a comprehensive picture of sediment depositional changes that may be linked to climate and environmental variability over the southern Arabian Desert. The chronology of the GBW core is provided by five radiocarbon (^{14}C) dates from terrestrial macrofossils (wood and twigs) extracted from sediment samples and indicates the core extends to ~900 CE. Our data indicates generally wetter conditions from 930 to 1400 CE corresponding to the "Medieval climate anomaly (MCA)" followed by arid phases during 1,410–1700 CE coinciding with the "Little Ice Age (LIA)". Evidence for a drier LIA include high authigenic calcium precipitation [Ca/(Al + Fe + Ti)], decreased TOC/TIC values, and gypsum precipitation, whereas the wetter MCA is characterized by higher detrital element ratios (Ti/Al, K/Al, Rb/Sr), and increased TOC/TIC and deposition of finer sediments (EM1). Furthermore, end-member mixing analyses (EMMA) derived from the grain-size distribution (EM2 and EM3) corroborates the deposition of coarser silt sediment through wind erosion and production of carbonate sand during the LIA concurrently with low lake levels under generally dry conditions. Aridity during the LIA is consistent with evidence and theory for weakened boreal summer monsoons during intervals of northern hemisphere cooling.

Keywords: lake sediment, paleoclimate, late holocene, Indian Summer Monsoon, XRF, Yemen, medieval climate anomaly, little ice age

INTRODUCTION

Large sub-tropical desert belts on Earth are formed due to a drastic decline in the distribution of rainfall that results from changes in atmospheric circulation (Edgell, 2006; Warner, 2009). Continuous terrestrial records located near desert margins (e.g., lacustrine, fluvial, cave and aeolian) have provided valuable insights into past climate and hydrological changes, which were often linked to fluctuations in the strength and latitudinal penetration of the summer monsoons (Singhvi and Kar, 2004; Sinha et al., 2006; Lespez et al., 2011; Wassenburg et al., 2016, among others). Lacustrine sediments, in particular, have provided valuable paleoenvironmental records from these regions (Abbott et al., 1997; Davies, 2006; Andersson et al., 2011) as they combine continuity with very high resolution. However, such records are only partially preserved or totally missing in the mid-and low-latitude desert belts.

Lakes situated near major global atmospheric circulation systems are likely to be highly susceptible to subtle changes in climate over time. The Arabian Peninsula is one of these locations as its northern areas are impacted by the Northern Westerlies Wind belt, while the southern margins are influenced by the Indian Summer Monsoon (ISM) circulation, with the latter linked to latitudinal changes in the Inter-Tropical Convergence Zone (ITCZ) position (Staubwasser et al., 2002; Gupta et al., 2003). Mechanisms influencing the current precipitation in the SW margins of the Arabian Peninsula are linked to shifts in the Red Sea Trough (RST), which is a low-pressure semi-permanent active zone over the Red Sea that generates local convective rainfall (Farquharson et al., 1996; Al-ameri et al., 2014). However, the precipitation pattern in the region is also modulated by the ISM, which brings moisture towards the southern Arabian Peninsula associated with northwards migrations of the ITCZ (Rodwell and Hoskins, 1996; Enzel et al., 2015). Holocene climate reconstruction from Yemen shows significant changes in the hydrological balance, probably as a response to the magnitude of monsoonal precipitation over time (Davies, 2006; Lézine et al., 2010; Berger et al., 2012). However, the existing lacustrine records are of relatively low temporal resolution. Other records, such as isotope data from speleothems, have proved to be valuable archives of climate change at high resolution, although with less continuity (Shakun et al., 2007; Fleitmann et al., 2011; Van Rampelbergh et al., 2013).

Hemispheric to global reconstructions have shown that warmth during the last two millennium reached a peak during the Medieval Climate Anomaly (MCA; from ~950 to ~1350 CE; Gayo et al., 2012), followed by increased cooling conditions during the Little Ice Age (LIA; ~1,500 to ~1800 CE; Matthews and Briffa, 2005; Miller et al., 2012), and anthropogenic post-industrial warming (Levitus et al., 2001). In fact, these two climate intervals (MCA and LIA) are defined in terms of temperature changes in the northern hemisphere; however, the temperature shifts in sub-tropical and tropical regions probably triggered changes in the moisture balance, which in turn gauged the amount and intensity of precipitation (Trenberth et al., 2003). The causes for the MCA and LIA have been widely discussed and linked to natural mechanisms, including solar and volcanic forcing as well as anthropogenic processes such as land cover decrease (Shindell et al., 2001; Ruddiman, 2013; among others). However, disagreement continues on the exact timing of both MCA and LIA intervals, which appear desynchronized worldwide (Crowley and Lowery, 2000; Broecker, 2001; Neukom et al., 2019), with many studies pointing to profound differences in temperature and precipitation gradients (e.g., Cronin et al., 2010; Jomelli et al., 2016). For example, while tropical East Africa experienced arid conditions during the MCA due to weak East African monsoons (Tierney et al., 2011), drier conditions associated with a positive phase of the North Atlantic Oscillation (NAO) characterizes the southern Levant during the same interval (Toker et al., 2012; Kushnir and Stein, 2019). Thus, there is a need to increase information density from climate archives around the globe to produce a reliable dataset for understanding the mechanisms and modalities of these two climate systems (MCA and LIA). The current study aims to enhance our understanding of the impact of these two climate phases by exploring sub-tropical hydrologic changes recorded in Gayal el Bazal, a lacustrine sedimentary sequence from southern Yemen, and it's the relation with tropical monsoonal circulation.

STUDY AREA

Gayal el Bazal is located in the town of Ghayl Ba Wazir, at 85 m above mean sea level, in the southern part of the Hadhramwat province, between the base of the Jabal Hasusah mountain cliffs and the Arabian Sea (**Figure 1A**). The geology of the region includes the Ghabar Group, which consists of metamorphic to anchi-metamorphic units, namely sandstone, greywacke, conglomerate, rhyolite, and quartzite rocks (As-Saruri and Wiefel, 2012). The region is characterized by several karstic sinkholes developed as a result of the dissolution of gypsum and limestone units from the Cretaceous Rus Formation (Hehmeyer et al., 2002). Lake Gayal el Bazal has occupied one of these sinkholes until very recently when it was reduced to small residual pools (**Figure 1D**), likely resulting from human groundwater withdrawal and agriculture. Currently, the small lake area (0.1 km^2, **Figure 1C**) is utilized by local communities for agriculture, mainly tobacco and palm plantations. The hydrological balance of the Gayal el Bazal is primarily controlled by summer precipitation (with an estimated mean of ~56 mm/yr) that falls over the main feeding Wadi Huwairah watershed (**Figure 1B**) and by an unknown amount of groundwater infiltration from the local aquifers. This limited precipitation amount promotes conditions of extreme pluvial events, with flash floods leaving a dramatic effect on local social and economic sustainability (Llasat et al., 2010). As for the water output balance, evaporation accounts for the sole estimated water output with unknown rates.

The climate of the studied area is characterized by extremely hot and dry conditions, with a monthly average ranges from 40°C to 43°C during summer and 28°C–31°C during winter (Bakhlah and Hassan, 2012). A hyper-arid desert dominates the east and north of our site (Almazroui, 2012), while the south part is slightly more temperate due to the Arabian Sea proximity (Hadden, 2012). Some minimal moisture appears to pass

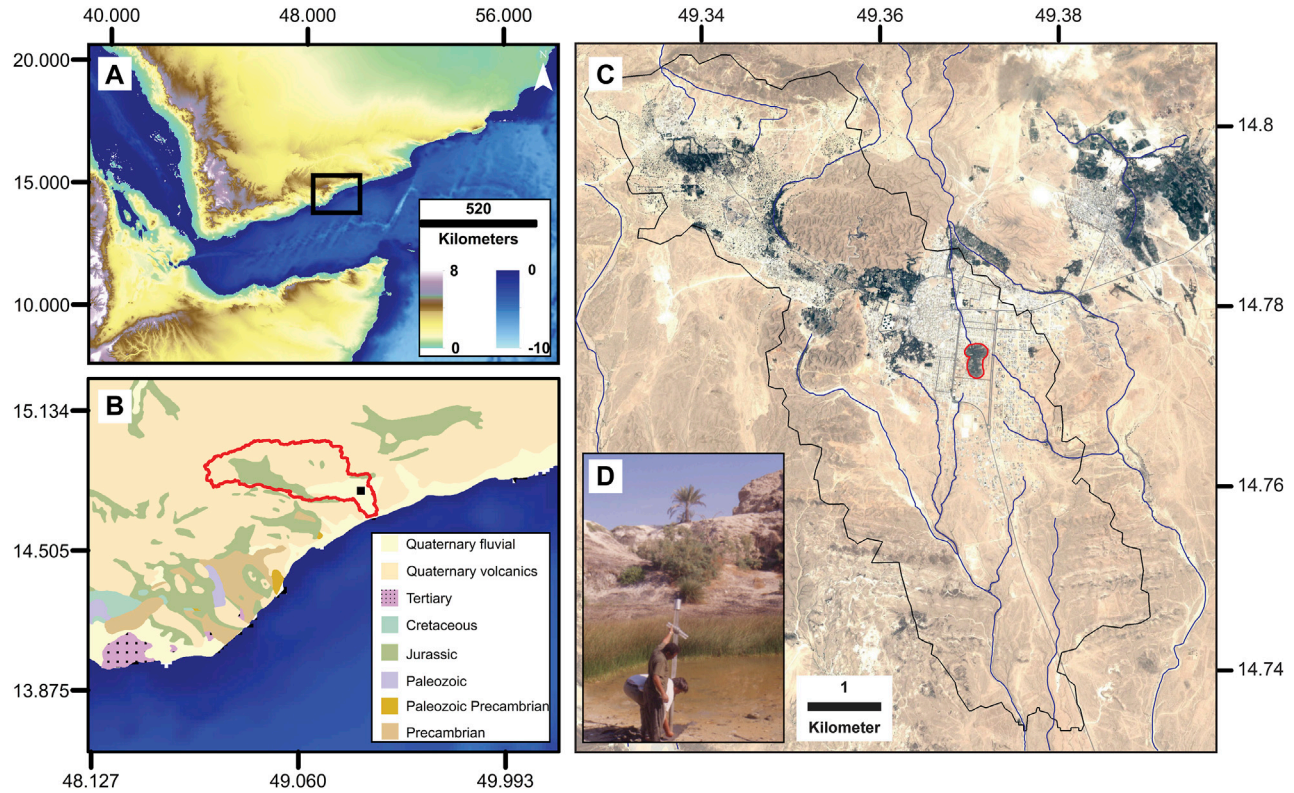

FIGURE 1 | (A) A SRTM 30 m elevation map of the SW part of the Arabian Peninsula with the studied area in Southern Yemen highlighted in a black square. **(B)** Geological map of the studied area marked in (a), highlighting the Wadi Huwairah watershed (red polygon) and the location of Gayal el Bazal (black square) (modified after Pollastro et al., 1999). The black square stands for the Gayal el Bazal area. **(C)** Detailed map of the Gayal el Bazal area. Black polygon marks the Gayal el Bazal Lake watershed with the riverine network system. The lake location is marked by a red polygon (Google Earth image, 2004). **(D)** Field photograph showing lake setting and core collection using Livingstone piston corer.

across the Hadhramaut Mountains to the north (that reach ~1,300 m) as a consequence of local orographic uplift and to reach the Arabian Desert, although the rates of this humidity are mostly unknown (Fleitmann et al., 2007). Most of the seasonal precipitation (~60%) over the region of Gayal el Bazal occurs during the spring months of March-April-May (MAM) through RST (**Figure 2B**; Baseer et al., 2019). During the summer season June-July-August (JJA), the moisture (~30%) is contributed by the ISM (**Figure 2C**; Fleitmann and Matter, 2009), and limited moisture is provided in the form of the winter season as a result of increasing outbreaks of North Westerly (NW) circulation (**Figure 2D**; Hasanean and Almazroui, 2015).

MATERIALS AND METHODS

Sample Collection

Three sites were cored in the Gayal el Bazal paleo-lake system aiming to retrieve a spatial coverage of the different sedimentary facies. The cores named Yemen-GBW01-2A (IGSN: CDR0000GK), Yemen-GBW01-2B (IGSN: CDR0000GL), Yemen-GBW01-3B (IGSN: CDR0000GM) were retrieved during a field campaign in December 2001 using a Livingstone piston corer, and cores measured 271, 95, and 108 cm (respectively) and were transported to the LacCore repository facility in Minnesota (United States) for curation and preservation.

Lab Measurements

Once in the lab, the cores were submitted to a set of non-destructive measurements, including magnetic susceptibility using a Bartington loop mounted to a Geotek multi-sensor core logger at a 5 mm (2.5 mm up and down) resolution and the data smoothed over 50 data points. Following this step, the cores were cut lengthwise into two halves (working and archive). While the archive halves were used for lithological description, imaging, and measurement of the elemental content using an ITRAX μX-Ray Fluorescence (XRF) core scanner, the working halves were used for destructive measurements (physical sampling). XRF measurements were done at a 0.5 cm resolution with the Cr and Mo tubes for identifying lighter and heavier elements, respectively (Croudace et al., 2006). The scanner generates element-related X-ray fluorescence peaks, and intensity is expressed in counts per second (cps), reflecting each given elemental concentrations (Löwemark et al., 2011; Rothwell, 2015; Chawchai et al., 2016). A semi-

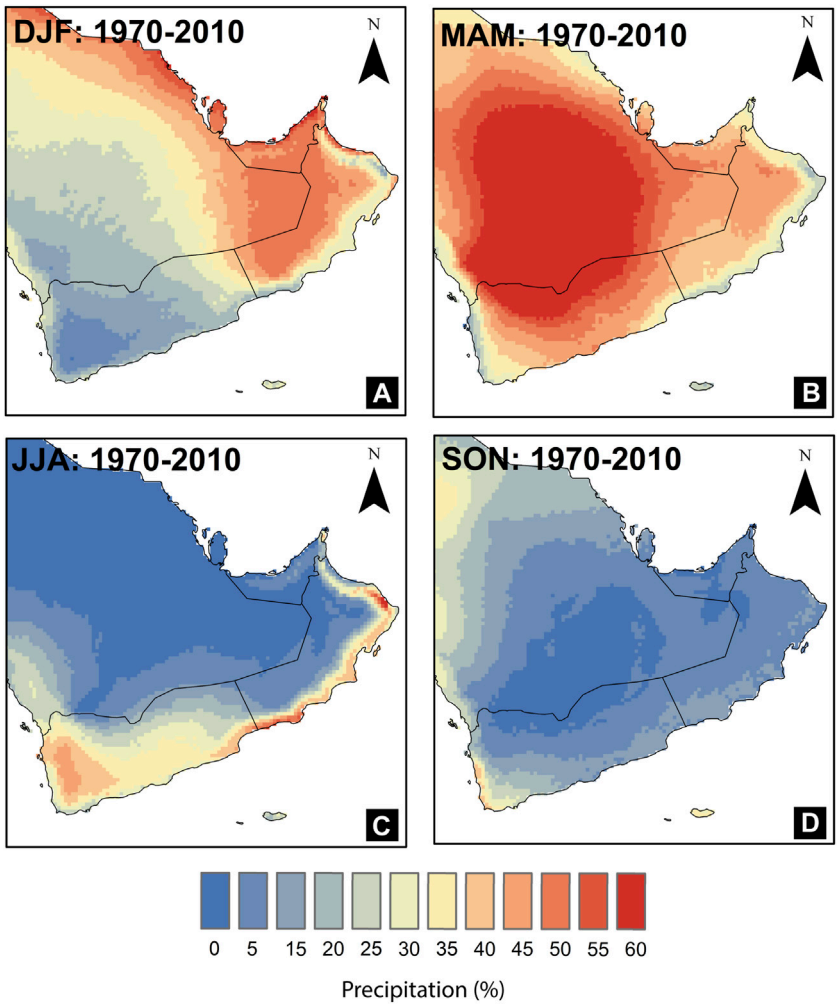

FIGURE 2 | The proportion of rainfall (1970–2010) by seasons: **(A)** winter (Dec-Feb), **(B)** spring (Mar-May), **(C)** summer (Jun-Aug), and **(D)** fall (Sept-Nov) (Source: WorldClim 2021).

quantitative analysis of the elements can be performed by normalizing element counts with total counts or Al to make a better comparison within intervals. Considering the parameters used during the XRF measurements, Al counts were reliable and were selected for normalization.

X-ray diffraction (XRD) measurements were carried out using a Rigaku Miniflex X-ray Diffractometer for the mineralogical study of the sediments. The mineral identification was carried out using PDXL 2 software, which uses a profile- and peak-based search approach based on detailed peak information. The quantitative analysis using reference intensity ratio determined the relative abundance of individual minerals.

Further destructive measurements include total inorganic and total organic carbon (TIC and TOC, respectively) at a ~3 cm resolution using a Skalar Primacs Series Total carbon analyzer. The samples were freeze-dried, weighed, and homogenized before the measurement. TIC was determined by acidification in the IC compartment at low temperature (100°C), which releases CO_2 to measure the abundance of inorganic carbon in the sediments. For TOC, dried sediments were treated with 1N HCl in order to remove carbonates, followed by heating the sample in the TC compartment at 700°C in the presence of pure Oxygen resulting in CO_2 releasing and generation of the abundance of organic carbon in the sediments.

Granulometric analysis was conducted using a Beckman Coulter LS 13 320 mw laser diffraction particle size analyzer on the same sampling resolution (~3 cm; n = 139). The sediments were pretreated with 10 ml H_2O_2 (30%) for organic matter removal and followed by acidifying using 1N HCl for removal of carbonate from the sediments (Murray, 2002; Vaasma, 2008). The solution containing digested sediments was washed with distilled water several times to remove the extra oxidizing reagents. The solution was homogenized with an ultrasonic bath prior to measurement. The grain size distribution was calculated for 100 grain size classes (particles sizes between 0.04 and 2000 μm), and the analytical error was less than 1%.

The chronology was established using AMS radiocarbon (^{14}C) dating carried out at Poznań Radiocarbon Laboratory, Poland, on

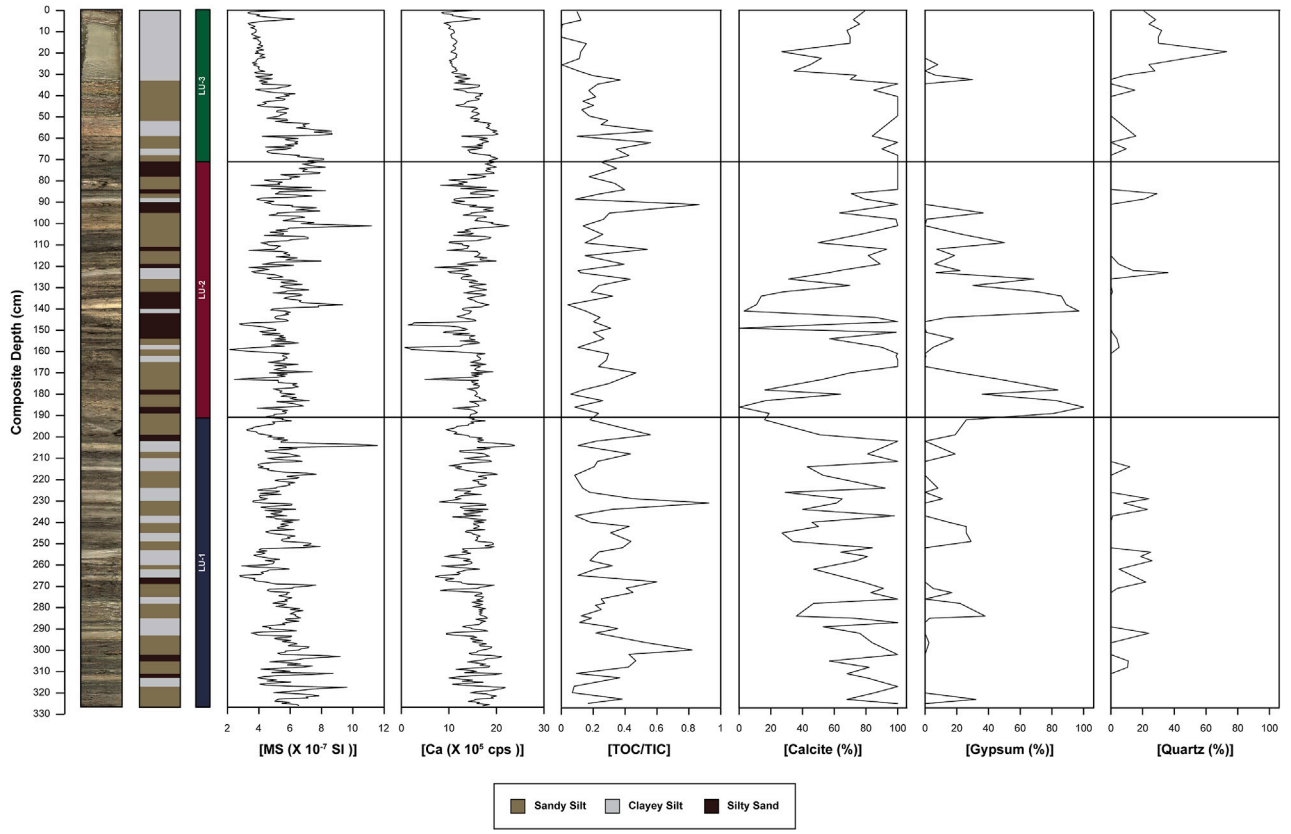

FIGURE 3 | The lithology of Gayal el Bazal sediment core showing the magnetic susceptibility (MS), the XRF (Ca counts), the XRD data (calcite, gypsum and quartz abundance), and TOC/TIC values.

wood and plant remains. Samples were selected from 5 different layers representing the whole composite core and weighed between ~5—15 mg for sufficient precision of ^{14}C dating. The raw AMS radiocarbon dates were calibrated using the OxCal program (Bronk Ramsey, 2009) with the most recent IntCal20 calibration curve (Reimer et al., 2020).

Statistical Approaches

For XRF data interpretation, a statistical approach was applied to understand possible grouping and disentangle complex signals out of the dataset. Further statistical analyses of the data [such as calculation of the principal component analysis (PCA)] were carried out using princomp function in R-Studio software (Mardia et al., 1979; Venables and Ripley, 2002). PCA is an important tool used for reducing the multivariate data into fewer dimensions and can help aid the interpretation of multiple elements. PCA transforms an original set of N-variables into a new set of N-principal components, which are orthogonal to each other (Xue et al., 2011). Each component is weighted in light of a linear combination of the original variables.

End-member mixing analysis (EMMA) was applied on the grain size parameters to understand the sediment mixtures in a series of sedimentary components (end members) reflecting the transport mechanisms and sediment sources (Dietze et al., 2012, 2013; Mishra et al., 2019). End member mixing analysis is a statistical tool that can disentangle the modes of transport of the sediments from polymodal particle size distribution (Weltje, 1997). The number of modes of transportation was selected based on a best-fit model for grain size distribution, representing the relation between the number of end members and the coefficient of determination (r^2). After optimizing all the parameters (n, q, l), the statistical analysis was performed using EMMA function based on *EMMA*geo-package, in R-language (Dietze et al., 2012).

RESULTS

Stratigraphy and Lithology

A composite core record was generated based on correlation of the different cores sequences and through a detailed identification of the same lithology units and layers in all sections. The composite core GBW reaches 3.26 m in length, and three different lithological units are established (LU-1 to LU-3) and distinguished by distinct sedimentary facies (**Figure 3**).

- *Unit LU-1* (326–191 cm) is characterized by clayey silt and sandy silt beds separated by minor erosional contacts. The

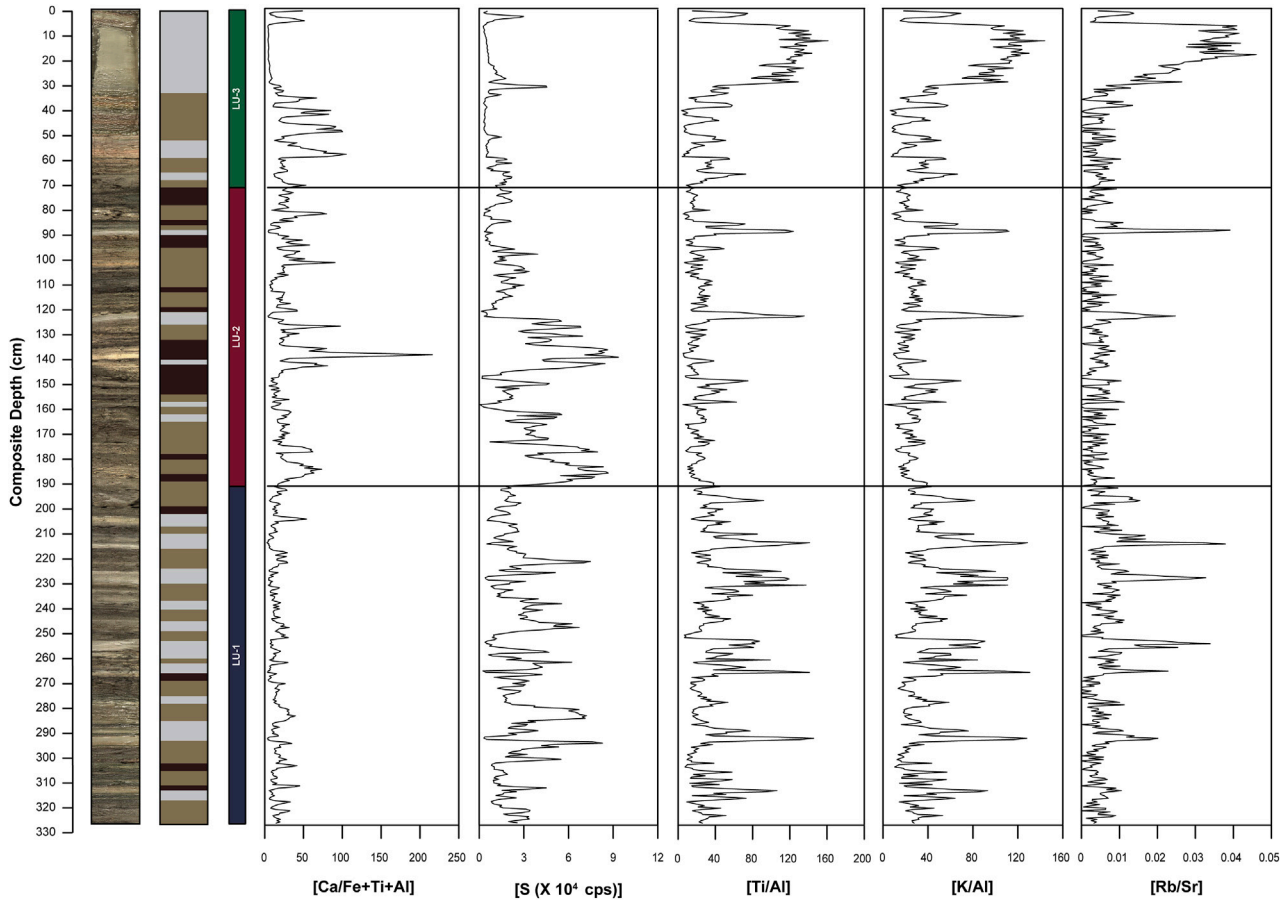

FIGURE 4 | Major XRF data presented in the paper and compared with a high-resolution core image of GBW. The elemental variability of Ca/(Al + Fe + Ti), S counts, Ti/Al, K/Al, and Rb/Sr is shown (see text for more details).

mineralogical composition is dominated by calcite which is the most abundant mineral (range 16–100%), followed by gypsum (0–38%) and quartz (0–26%). There are increases in quartz minerals at 217–208 cm, 267–250 cm, and 295–286 cm intervals; **Figure 3**. The MS values in LU-1 range from 2.78 to 11.57 × 10^{-7} SI and average ~5.46 × 10^{-7} SI. MS decreases at 326–265 cm and 251–224 cm and increases from 205 to 200 cm, where the highest values are observed for this unit (**Figure 3**). The Ca abundance displays a similar pattern or curve with MS values for those intervals (r = 0.93; **Figure 3**). TOC/TIC content in the LU-1 unit varies between 0.07 and 0.92, with higher values of TOC/TIC in specific layers (217–208 cm, 237–222 cm, 267–250 cm, and 295–286 cm) (**Figure 3**).

- U*nit LU-2* (191–71 cm) is marked by silty sand and sandy silt and the appearance of gypsum. The sediments in the unit mainly contain calcite (0.4–100%) and gypsum (0–100%) abundance minerals with a trace amount of quartz (0–36%). The MS values range from 2.5 to 11.2 × 10^{-7}SI with an average of 5.7 × 10^{-7}SI, and higher values are for intervals from 102 to 99 cm, 136–139 cm. The higher value of MS is also marked by higher values of Ca counts, coarser grain size (silty sand layers), and increased gypsum abundance (**Figure 3**). TOC/TIC values range from 0.04 to 0.86 and average 0.25 in the LU-2 unit. Lower TOC/TIC are observed for intervals 98–93 cm, 146–126 cm, and 191–174 cm (**Figure 3**). The LU-2 unit is also marked by deposition of clayey silt sediments at 90.5–87.5 cm and 125–121 cm (**Figure 3**).
- *Unit LU-3* (71–1 cm) consists of clayey silts and sandy silts with abundant quartz compared to the rest of the sequence. Specifically, the interval 29–1 cm is marked by a clayey silt bed with increased quartz mineral for that interval (**Figure 3**). The MS values fluctuate from 3.3 to 11.2 × 10^{-7} SI and average ~5.34 × 10^{-7} SI. Lower values of MS are observed from interval 29–1 cm (**Figure 3**). TOC/TIC content in this unit varies between 0.23 and 0.57 and showing lower values of TOC/TIC are observed from 63 to 50 cm (**Figure 3**).

Geochemistry and Statistical Analysis

XRF analyses document considerable variations in the counts for major elements like Al, Si, S, Cl, K, Ca, Ti, Mn, Fe, Sr and minor elements like Rb and Zr, which we interpret to reflect

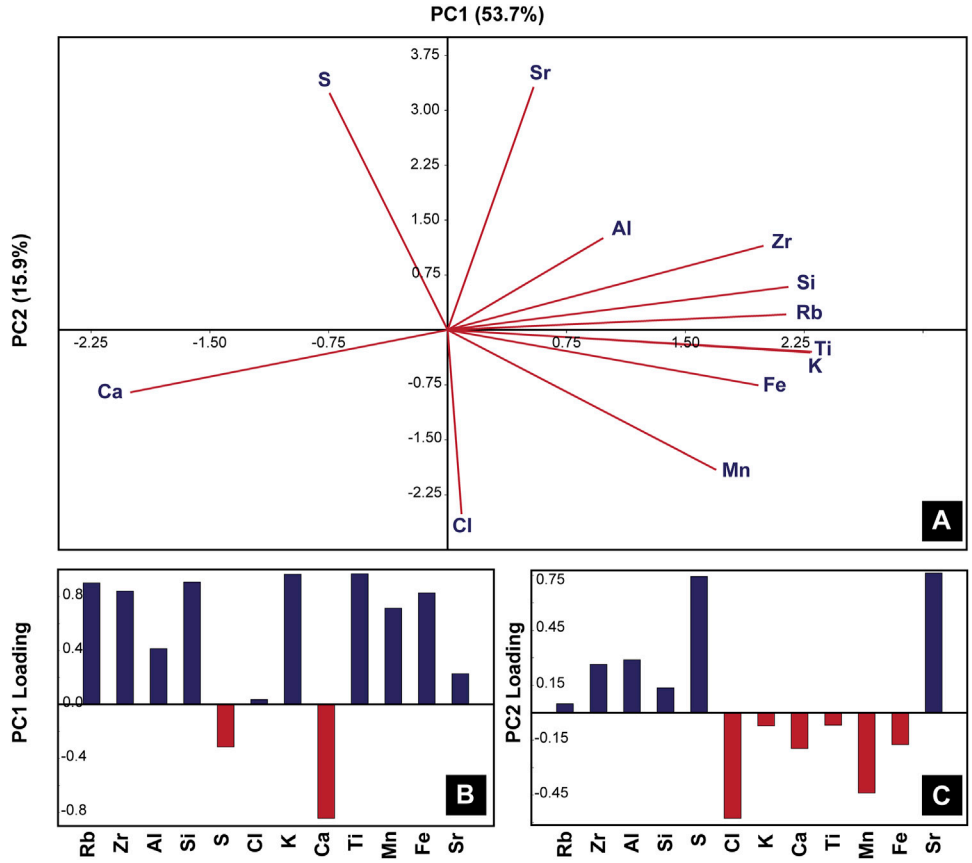

FIGURE 5 | Statistical analyses of the XRF data. **(A)** Principal Component Analysis (PCA) and biplot between PC1 and PC2 showing the geochemical parameters of composite core GBW. **(B)** Loadings of principal components (PC1) derived from elemental data. **(C)** Loadings of principal components (PC2) derived from elemental data.

relative abundance changes. Element abundance and ratios like Ca/(Al + Fe + Ti), S counts, Ti/Al, K/Al, and Rb/Sr show significant variability through the whole GBW composite core (**Figure 4**). The element ratios like Ti/Al, K/Al, and Rb/Sr exhibits similar stratigraphic patterns. Unit LU-1 records the higher values of Ti/Al, K/Al, and Rb/Sr from 217 to 208 cm, 237–222 cm, 267–250 cm, and 295–286 cm (**Figure 4**). Unit LU-2 also shows sharp spikes in Ti/Al, K/Al, and Rb/Sr from 90.5 to 87.5 cm and 125–121 cm (**Figure 4**). However, Ca/(Al + Fe + Ti) sharply increases at 98–93 cm, 146–126 cm, and 191–174 cm and higher values of S counts from 126 to 146 and 162–191 (**Figure 4**). In Unit LU-3, Ti/Al, K/Al, and Rb/Sr increases from 35 to 1 cm. Additionally, Ca/(Al + Fe + Ti) shows increase trend interval between 59–34 cm (**Figure 4**).

The principal component (PC) analysis reveals two components explaining ~69% variability in the dataset (**Figure 5A**). PC1 receives positive loading from Ti, K, Fe, Si, Rb, Al, and Zr and negative loading from Ca (**Figure 5B**). The PC2 has positive loading from S and Sr but negative loading from Cl (**Figure 5C**). The biplot of PC1 and PC2 shows elements like Ti, K, Fe, and Rb are oppositely associated with Ca, Sr, and S (**Figure 5A**).

Grain Size Distribution and Statistical Approach

The clastic grain size distribution of the GBW composite core is largely characterized by silt with minor variations of sand and clayey silt fractions. The mean grain size of the core ranges from 3.1 to 7.1 ϕ and the coarsest grain size fraction is found at 152–144 cm and finest fraction at 260 to 253 cm (**Figure 6**). The overlay of all grain size data from all samples revealed a polymodal distribution, and hence end-member analysis has been applied. The EMMA of grain size distribution in GBW core yielded an optimal model with five end members and explained 65% variability of the total dataset. End member 1 (EM1) represents the finest particle fraction in the core with the dominant modal grain size of 7.1 and is in the range of clayey silt. For EM2, the dominant modal grain size is 4.8 and lies in the range of medium to coarser silt. Furthermore, EM3 (mode = 3.2 ϕ), EM4 (mode = 1.4 ϕ) and EM5 (mode = 0.65 ϕ) are in the range of fine, medium and coarse sand, respectively. Unit LU-1 is marked by the increased relative abundance of EM1 from 216 to 209 cm and 269–265 cm and a higher abundance of EM2 between 278–276 cm and 305–296 cm (**Figure 6**). Unit LU-2 represents higher contribution from EM3, EM4 and EM5 for

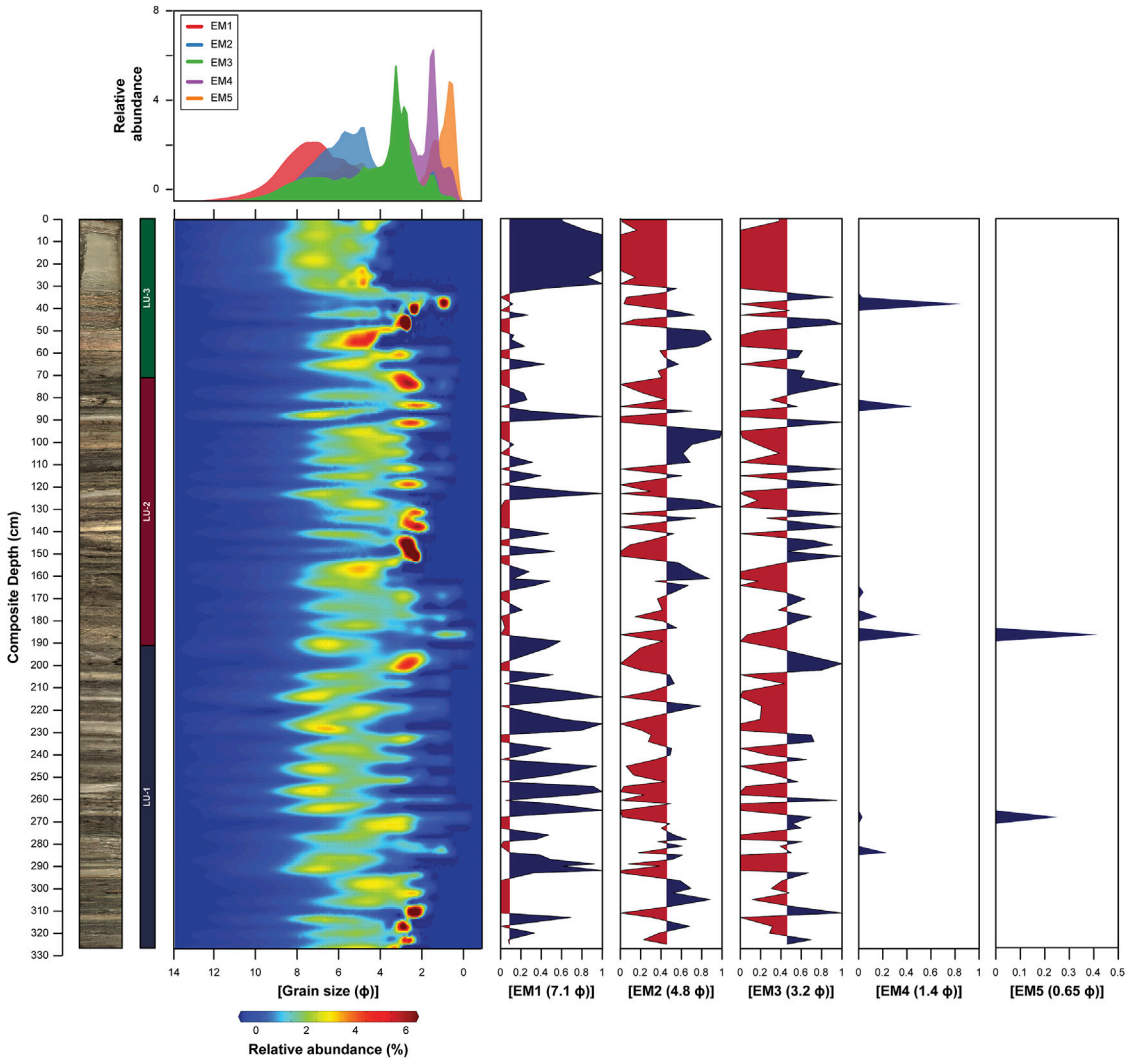

FIGURE 6 | Overlay of the grain size distribution of all samples and particle distribution through down-core sediments and five end members with their relative abundance plotted against the composite depth.

intervals ~86–84 cm, 175–167 cm, 180–178 cm, 189–186 cm and significant contribution from EM2 for 109–95 cm, ~118–115 cm, ~129–126 cm, and 161–158 cm (**Figure 6**). Unit LU-3 has pronounced contribution from EM1 from 29 to 1 cm and EM2 from 57 to 50 cm. For EM3, EM4, and EM5, representing coarser particle size fractions are higher for 41–35 cm in the unit (**Figure 6**).

Chronology

The age model for GBW is based on five accelerator mass spectrometry (AMS) radiocarbon dates on terrestrial fragments (wood, twig, and plant remain) picked from intervals 62, 112, 157, 242, and 325 cm depth of the GBW composite core. The radiocarbon dates can also be affected by the reservoir effect, which can skew results such that older radiocarbon ages can appear than the equivalent age of the sample (Philippsen, 2013). However, in the GBW composite core, radiocarbon ages are based on the most reliable material, including terrestrial macrofossils (short-lived twigs remains) for younger sediments in the lake (Marshall et al., 2007). Calibration of obtained ^{14}C dates was done with the IntCal20 calibration curve (**Table 1**; Reimer et al., 2020), and the age-depth model was carried out using a Poisson process model deposition (P_Sequence; Ramsey, 2008) (**Figure 7**).

DISCUSSION

Variability of Allochthonous vs Autochthonous Depositional Patterns in GBW

The elemental analysis documents a series of processes occurring in the lake environment, including changes in the origin and

TABLE 1 | Radiocarbon ages for the GBW core based on OxCal calibration (Reimer et al., 2020).

Composite Depth (cm)	*AMS ^{14}C (BP)*	*Calibrated ^{14}C (CE)*	*Error*	*Lab no*
62.5	200 ± 30	1768	30	Poz-127874
112.5	370 ± 30	1,565	30	Poz-120224
157.5	400 ± 30	1,481	30	Poz-127875
242.5	675 ± 30	1,326	30	Poz-120852
325.5	1,140 ± 30	914	30	Poz-120852

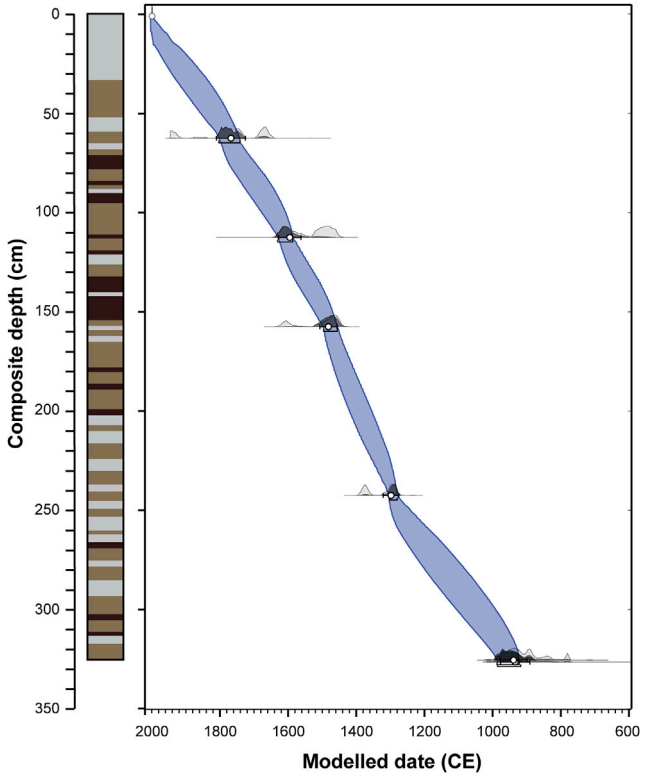

FIGURE 7 | Age-depth model for the GBW core with grey lines indicating confidence limits and blue curve showing age-depth interpolation.

provenance of particles (e.g., allochthonous vs autochthonous), oxidation/reduction conditions in the lake bottom, water velocities and depth variabilities through time (Engstrom and Wright, 1984; Zolitschka et al., 2002; Boyle, 2005; Weltje and Tjallingii, 2008; Löwemark et al., 2011). These can in turn, reflect changes in climatic and limnological conditions. We interpret that the inorganic geochemical compositions of the GBW core are primarily controlled by both allogenic processes (fluvial (wadi) discharge and aeolian input) coupled with authigenic processes (i.e. precipitation of evaporite minerals).

The statistical analyses of the elemental record (PC1) carried out on the XRF data show that Ti, K, Si, Rb, and Zr follow the same behavior, with elements like Mn and Fe partially following the same positive axis (**Figures 5A,B**). Previous studies carried out on similar settings points that Ti and K are geochemically stable lithogenic elements, which are hosted by resistant minerals and are conservative in most geochemical environments, and thus reflect detrital input into the lake (Boës et al., 2011). Changes in the concentration of Ti and K can be related to either stronger catchment runoff, which reflects wetter conditions, or enhanced aeolian deposition, hence a low precipitation regime (Hou et al., 2017). In the studied core, we observe a direct association of Ti and K with the clayey silt or finer fraction (EM1) of the sediment (r = ~0.78, **Figure 8**) and hence these elements probably represent detrital origin. Many studies done in lakes dominated by the siliciclastic type of sedimentation have shown that Fe and Mn can originate from detrital input and catchment runoff, though they can often be related to redox conditions in the sediment/water interface (Davison, 1993). Therefore, interpretation of their temporal behavior in the depositional system should carefully be considered in light of variability occurring in the other measured elements. In GBW, PC1 data reveals that Fe is aligned with detrital elements (Ti, K); hence we estimate that it also represents an allogenic provenance (**Figures 5A,B**). Although many studies use Si to estimate diatom blooms (Schettler et al., 2006), which may occur during episodes of increase in nutrient input from aeolian transport or volcanoclastic materials (Peinerud, 2000) however, our statistical analysis shows a close association of Si with Ti and K, which is carried by the silicate fraction and may indicate a terrigenous source for Si (**Figures 5A,B**).

Rb appears to be associated with fine-grained siliciclastic rocks (Kylander et al., 2011). In our core, this element shows a positive correlation with Al and K (**Figures 5A,B**); hence can be used to measure the amount of siliciclastic material depositing in the basin. The Rb/Sr ratio is often associated with the chemical weathering of catchment rock and can be interpreted as the changes in fluxes of dissolved materials within from catchment (Miriyala et al., 2017). This behavior suggests positive loading on PC1 indicates detrital influx into the lake system. Ca is on the negative axis of PC1, and hence we estimate that it shows a non-detrital origin; therefore, it indicates authigenic processes occurring in the lake (**Figures 5A,B**) (Zhao et al., 2010). We, accordingly, suggest that the elemental ratios of Ti/Al, K/Al, and Rb/Sr (or PC1 score) are well suited for estimating changes in the terrestrial sediment supply through time and can hence be used to reconstruct past fluvial discharge (Neugebauer et al., 2016).

PC2 is defined by positive loading of Sr and S and negative loading of Cl (**Figure 5C**); hence this principal component appears to indicate *in-situ* precipitation of carbonates. Moreover, Ca indicates authigenic origin due to its negative loading with PC1 (**Figure 5B**) and has no major correlation with S and Sr (**Figure 5C**). However, there is a possibility of allogenic sources of Ca to the lake basin cannot be omitted, and could consist of both fluvial and aeolian origins. Detailed XRD

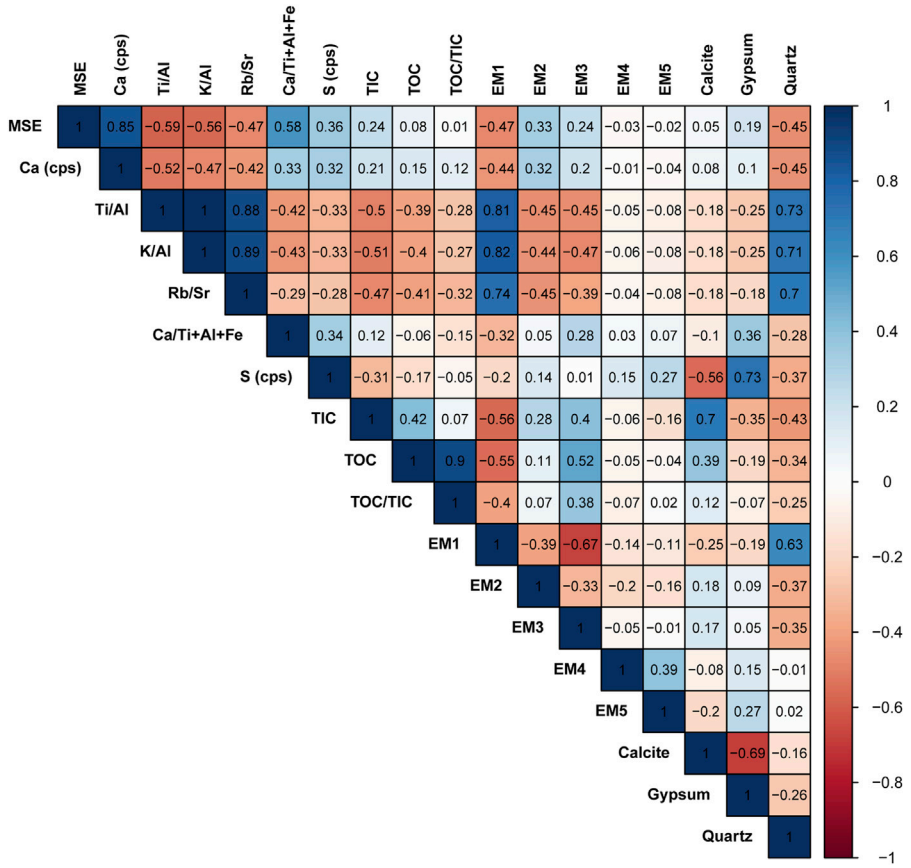

FIGURE 8 | A Pearson correlation matrix of elemental abundance and ratios, mineral abundance, different end members of grain size, MS, and TOC/TIC data of the GBW composite core.

measurements reveal that the GBW core contains calcite and gypsum, with the occasional appearance of quartz. The studies also show that calcite might constitute a major percentage of dust particles in the Arabian desert (Al-Dousari and Al-Awadhi, 2012; Al-Dousari et al., 2013). In general, Ca represents an arid environment; hence, to estimate the authigenic deposition of Ca, the ratio between Ca/(Al + Fe + Ti) might represent a reliable proxy of precipitation changes in the region (Mueller et al., 2009). Higher values of this ratio can imply an increase in lake water salinity coupled with lower runoff from the catchment, which might point to dry conditions. S counts show a good correlation with gypsum abundance (r = 0.73, **Figure 8**), and their down-core shifts in the sediment can be associated with lower lake levels or shallow water depths, indicating dry climatic conditions in the region.

Correlation of Magnetic Susceptibility, Total Inorganic Carbon/Total Organic Carbon With Elemental Proxies

The magnetic susceptibility (MS) properties of sediments are influenced by the presence of Fe-bearing ferromagnetic minerals and serve as a proxy to disentangle the abundance of paramagnetic and diamagnetic minerals, such as carbonates, quartz, and clays (Bareille et al., 1994; Schnurrenberger et al., 2003). Previous studies have shown that MS can be a reliable indicator of both external processes (e.g., weathering magnitude and volcanism) and internal chemical cycling in the lacustrine environment, particularly the oxidation state in the sediment-water interface that can influence magnetite dissolution or formation (Rawat et al., 2021). In GBW, MS values are relatively low (averaging ~5.6 × 10^{-7} SI) compared to carbonate rich lakes (Wünnemann et al., 2010; Pleskot et al., 2018), which can be associated to an increase in the presence of diamagnetic minerals or due to presence of negative magnetic susceptibility values of rocks in the catchment area (e.g. sandstone, greywacke, conglomerate, quartzite and carbonates). The MS values in the GBW sediments are mainly controlled by the minerals of Ca in the sediment as a high correlation is observed between Ca counts and MS values (r = 0.82, **Figure 3** and **Figure 8**). Our GBW core is highly enriched in calcite (a typical diamagnetic mineral) with frequent intercalations of gypsum (least diamagnetic mineral), and we find that the layers enriched by gypsum have relatively higher values of MS compared with those enriched by calcite (Ivakhnenko et al., 2015). Furthermore, studies have shown that sediment consisting of higher carbonate or organic matter can dilute the concentration of magnetic minerals, also leading to low MS values

(Hounslow and Maher, 1999). In several previous studies, MS values have been shown to increase with decreasing grain-size fraction (Thompson and Morton, 1979; Dessai et al., 2009). However, in GBW high values of MS are not necessarily associated with changes in the grain size distribution. The MS values are also lower for higher detrital influx events where quartz is found due to its diamagnetic properties, however it doesn't show any significant variation throughout the GBW core.

The Total Carbon (TC) budget of a lake is primarily controlled by chemical and biochemical processes associated with the balance between the water input and the evaporation of lake water (Håkanson and Jansson, 1983). TIC is primarily controlled clastic sediment input or precipitation/evaporation processes, depending on whether carbonate minerals are allogenic or authigenic. In turn, TIC can serve as a proxy for temperature and precipitation changes (Yanhong et al., 2007). We estimate that TIC values increases during drier conditions due to the increased carbonaceous dust influx as it correlates quite well with calcite mineral abundance (r = 0.7). Hence for those intervals, lower values of TOC/TIC reflect intervals with sandy silt units. TOC indicates the productivity of the lake, oxic state of the bottom waters and can also be used to track changes in the organic deposition conditions through the sedimentary sequence (Chen et al., 2001; Xu et al., 2007). The organic matter in the lake can be derived from the allochthonous input through catchment runoff or wadi influx and from autochthonous sources. However, in general, low productive lakes get the significant contribution of organic matter from the allochthonous terrestrial sources (Dean and Gorham, 1998). Hence, the primary source of TOC for the paleo-lake Gayal el Bazal is the terrigenous sediment supply during the relatively wetter condition in the region. The TIC and TOC data thus are complex to interpret due to uncertainty in the sources of these materials to the sediment through time. Nevertheless, the TOC/TIC data used in conjunction with other proxies (e.g., Ti/Al, K/Al, and Rb/Sr or PC1 score) provide information about different sedimentary processes, such as fluvial vs. aeolian input to the lake, and thus reflect rainfall changes. We further suggest that the high preservation conditions of the organic matter result from relatively fast burial processes, which in turn might indicate deposition during intense floods.

Deposition and Transport Mechanism of Sediments

The depositional patterns of lake sediment are controlled by sediment transport mechanisms such as fluvial inflows, aeolian transport, and turbid inflows (Solohub and Klovan, 1970; Sly, 1994; Lou et al., 2000; Stuut et al., 2002). These different transport mechanisms and depositional conditions can yield high variability in grain size distribution and grain morphology (e.g., sphericity and roundness; Håkanson and Jansson, 1983; McLaren and Bowles, 1985; Sun et al., 2002; Last, 2005; Vandenberghe, 2013). Processes like these can create complex distributions in the particle size variation; thus, disentangling the sources is a must. To un-mix the modes of deposition into the lake system, end-member mixing analysis (EMMA) is applied to provide meaningful end members associated with various depositional processes. This approach, applied on the GBW core, resulted in five particle populations of modes attributed to different transport mechanisms. EM1 is the finest grain size fraction (7.1 ϕ), which a large majority falls under the clayey silt class and reflects the fluvial or *wadi* influx into the lake. Previous studies have shown that during pluvial events in arid environments, clayey silt is deposited in the basin, mostly due to surface runoff (Lézine et al., 1998, 2007). Furthermore, heavy elements (e.g., Ti, K, and Rb) and PC1 score are closely associated with EM1 variation, which are introduced to the basin also through surface runoff (r = ~0.8; **Figure 8**). Hence, finer fraction EM1 along with other proxies (detrital elements and PC1) are interpreted as increased precipitation in the region. EM2 consists of medium to coarse silt (4.8 ϕ) and reveals the aeolian mode of transport of sediments into the basin. It is consistent with available records showing that the southern Arabian Peninsula is highly influenced by aeolian processes (Khalaf and Al-Hashash, 1983; Al-Dousari et al., 2013). The greater abundance of EM2 reflects coarser aeolian dust advected from proximal sources, as it is larger in size than the dust particles from distal source (Crouvi et al., 2008). EM3 is situated around a fine sand fraction (3.1 ϕ) which would have formed due to the lowering of lake level or shallow near the shore. Hence, this end member, along with increased authigenic Ca precipitation (Ca/(Al + Fe + Ti)) in the lake, represents dry episodes with shallow water conditions, characterized by higher hydraulic energy conditions and deposition of coarser sediments in the lake. The greater abundance of EM3 is attributed to lower lake stands that probably resulted from periods of increased aridity and decreased water supply from the wadi catchment. EM4 (mode = 1.4 ϕ) and EM5 (mode = 0.65 ϕ) represent the coarsest sediment fraction and indicate extreme erosional events. Those intervals with a high abundance of EM4 and EM5 are followed by a higher abundance of EM1 (clayey silt). Hence we suggest that these two end members are indicative of coarser erosional material from the catchment.

Unraveling the Medieval Climate Anomaly and Little Ice Age in Yemen

The sedimentary record from the GBW core reveals the past 1,200 years' climatic changes in the southern Arabian Peninsula and is divided into three stages based on the down-core variation (**Figure 9**).

Unit LU-1 (~920–~1400 CE)

Unit LU-1 is dominated by detrital influx to the lake, as is marked by a higher PC1 score and an increase in TOC/TIC interpreted as resulting from augmentation in catchment runoff during pluvial episodes (**Figure 9**). The intervals from 930–1000 CE, 1,060–1110 CE, 1,140–1200 CE, 1,220–1280 CE, and ~1,330–1400 CE are sustained periods of wetness as represented by increased catchment erosion and augmentation of the clayey silt fraction (EM1 score) (**Figure 9**). These periods coincide with the Medieval Climate Anomaly (MCA; ~900–1350 CE; Gayo et al., 2012), which is an interval characterized by a shift in atmospheric circulation in the northern hemisphere that has left signals in sedimentary archives around the globe (Graham et al., 2011;

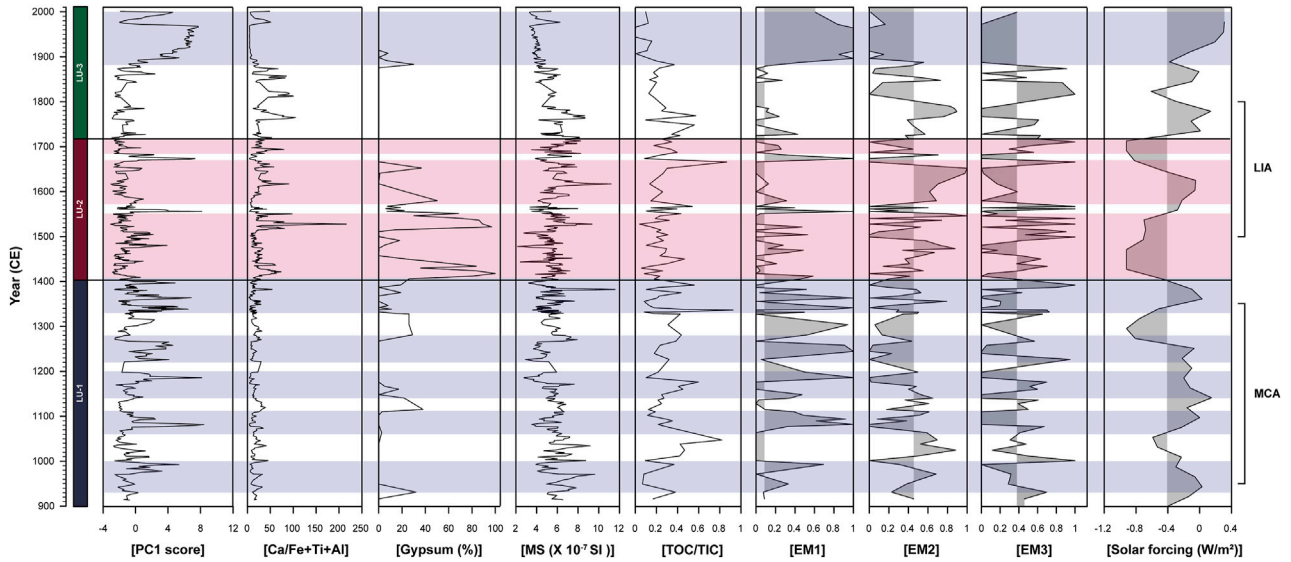

FIGURE 9 | Multiproxy data obtained from Gayal el Bazal from 900 CE to 2000 CE showing three units (marked by blue and red stripes) indicating wet and dry intervals, respectively (Steinhilber et al., 2012).

Lüning et al., 2018). The synchroneity and extent of the climate pattern during this period are debated (Mann et al., 2009), yet it is widely recognized as a relatively warming interval in the northern hemisphere. However, it appears that the MCA interval in our record does not uniformly represent wet conditions but shows the inception of a major wet interval probably associated with increase warmth and humid conditions. Enhanced precipitation in the region during the MCA is consistent with regional records (Gupta et al., 2003; Fleitmann et al., 2004). The possible causes of the MCA are debatable as different forcing mechanisms, such as solar, volcanic, greenhouse gases, and land cover/use changes, occurred individually, and their combination all likely influenced this climatic shift. The simulation provided by Community Earth System Model-Last Millennium Ensemble (CESM-LME) captures globally warmer conditions during the MCA due to weaker volcanic forcing relative to radiative forcing that characterized the Little Ice Age (LIA; ~1,500–1800 CE, Otto-Bliesner et al., 2016). Fluctuations in the regional climate during the MCA can also be attributed to changes in the intensity of solar irradiance and thus inducing enhanced wet conditions in the region, which led to an increase in the input of allogenic materials into the lake (**Figure 9**). We estimate that this anomaly could have been triggered by the northward migration of the ITCZ linked to increased solar forcing (Broccoli et al., 2006; Kuhnert and Mulitza, 2011), which led to an increase in humidity in the southern margins of the Arabian Peninsula during the MCA.

Unit LU-2 (~1,400–1720 CE)

The LU-2 unit is defined by increased Ca/(Al + Fe + Ti), gypsum abundance, and higher EM2 abundance, which we believe represent an increase in the evaporite formation and aeolian influx to the lake basin. During 1,410–1450 CE, 1,500–1580 CE, and 1,640–1690 CE, higher values of Ca/(Al + Fe + Ti) and increased abundance of gypsum indicate periods of decline in lake level, which exemplify for dry climatic conditions in the region (**Figure 9**). In fact, the EM2 abundance from 1,430 to 1670 CE significantly increases due to drier conditions. These dry episodes appear to prevail during the LIA when coarser silt sediments were brought into the lake and were consequently winnowed under lower lake levels. Aridity during the LIA is consistent with regional evidence (Felis et al., 2018) and follows proposed theories for weakened boreal summer monsoons during an interval of northern hemisphere cooling (Feng and Hu, 2008; **Figure 9**).

Conversely to the MCA interval, with a southward migration of the ITCZ during the inception of the LIA, an increase in the interhemispheric temperature contrast and enhanced high-latitude ice cover resulted in arid climatic conditions on the southern margins of the Arabian Peninsula (Schneider et al., 2014). Hence precipitation changes in Yemen during both the MCA and LIA anomalies were possibly driven by changes in the mean position of ITCZ. However, we infer that the LIA was not extremely dry, as we do not see evidence for compete desiccation of the lake and formation of soils.

Unit LU-3 (~1720–2000 CE)

This unit consists of post-LIA sediments and is defined by higher detrital input to the lake post-1900 CE. These intervals are defined by higher values of PC1 score and finer sediment (EM1 score) fraction but lower values of TOC/TIC (**Figure 9**). The unit is also marked by a higher aeolian influx due to an increase in the abundance of EM2 (**Figure 9**). However, uncertainty in our age-depth model is high for this section, as it is difficult to accurately constrain the timing of initial influx of detrital material to the lake. However, it occurred after the LIA and is marked by the inception of wetter conditions. Several

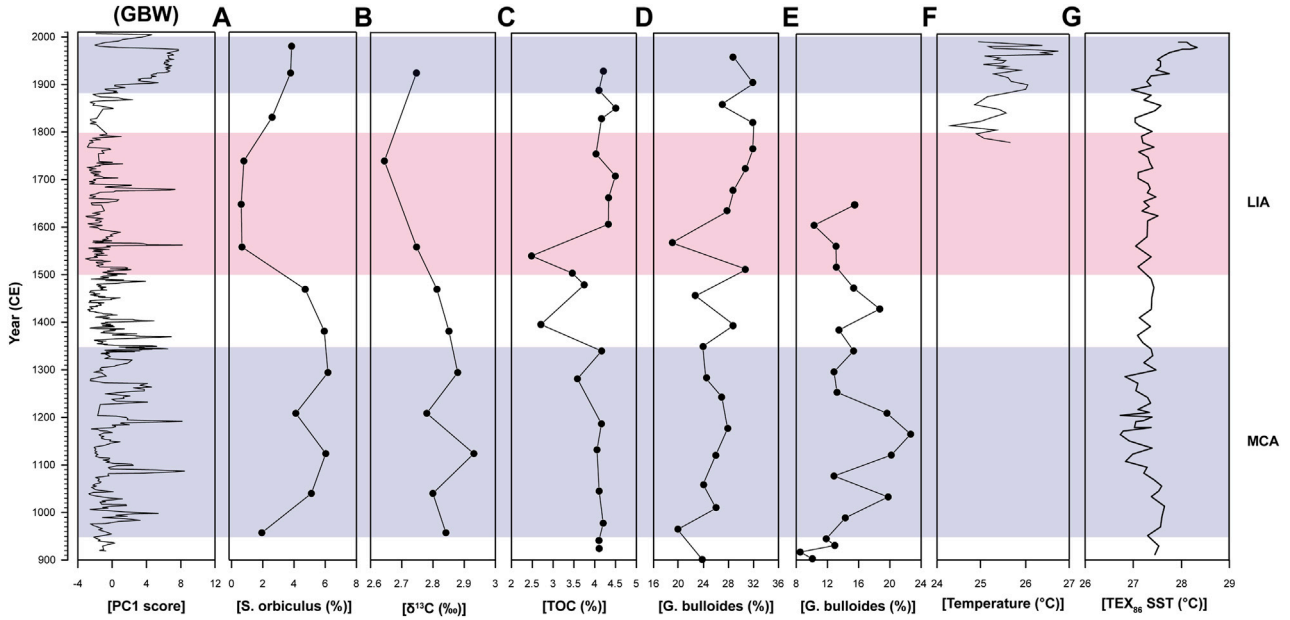

FIGURE 10 | Comparison of the GBW record with other regional paleoclimatic data. **(A)** $\delta^{13}C$ and **(B)** TOC, both from Shuaiba Lagoon (Saudi Arabia; Abu-Zied and Bantan, 2015), **(C)** TOC values from Naro Moru Tarn (Mount Kenya; Fastook et al., 1999), **(D)** G. Bulloides from core RC2735 (Anderson et al., 2010) and **(E)** G. Bulloides from core ODP Hole 723A (Gupta et al., 2003), both from the Arabian Sea (Oman margin). **(F)** TEX86 temperature reconstruction from Lake Turkana (Berke et al., 2012). **(G)** δD_{wax} data for the past millennium from a Gulf of Aden core (Tierney et al., 2015).

studies have reported warm and wet conditions following the LIA (Kotlia et al., 2012; Lüning et al., 2019), and our GBW record follows a similar trend. We suggest that this pattern is promoted by an active Red Sea Trough system that enhances precipitation over the southern Arabian Peninsula (Almazroui, 2012; Baseer et al., 2019).

Climate Variability in the Region

Based on the multiproxy approach of this study, high rainfall intervals were identified during ~930–1400 CE, with lower magnitudes occurring during ~1,410–1700 CE (**Figure 9**). A similar precipitation trend is witnessed in other well-dated sites from NW Arabia and eastern Africa, suggesting warm and humid conditions during the MCA followed by a cold and dry condition during the LIA (Lüning et al., 2017). A late Holocene study from Shuaiba Lagoon, Saudi Arabia, reveals high paleo-tidal elevation as shown by enrichment in $\delta^{13}C$ and δD of *Sorites orbiculus* indicating wet climatic condition during 1,000–1550 CE followed by aridity from 1,550 to 1850 CE due to MCA and LIA influence in the region (**Figure 10A**; Abu-Zied and Bantan, 2015). Furthermore, marine records retrieved on the Arabian Sea also report increased monsoonal activity 750–1150 CE and a weaker monsoon during 1,350–1550 CE (**Figures 10D,E**), which correlate well with two large temperature excursions during the late Holocene (Anderson et al., 2010). Additional records from Mount Kenya (**Figure 10C**) and Lake Turkana (**Figure 10F**) report cooler on average temperatures during the LIA but no indication of the MCA (Fastook et al., 1999; Berke et al., 2012). In contrast, a study based on sea surface temperature (SST) reconstruction from the Gulf of Aden using GDGTs shows no major indication for substantial temperature change during the MCA and LIA (**Figure 10G**; Tierney et al., 2015). This pattern can potentially be arguable due to major cold upwelling in the Arabian Sea that results from stronger Indian Summer Monsoons (SW winds) that brings colder, nutrient-rich waters from the Indian Ocean. The relationship between cold upwelling conditions during higher solar irradiance was already established by a previous study from the Oman margin (**Figure 10E**; Gupta et al., 2005), showing strong SW monsoons during the MCA (equivalent to a solar maxima interval) and weaker strengths during the LIA (solar minima). Hence, both climatic anomalies are well documented in many segments of East Africa, Saudi Arabia, and the Arabian Sea which most likely are triggered by changes in solar and volcanic forcing and ocean cycles.

CONCLUSION

This study integrated magnetic susceptibility, geochemical, and TOC/TIC analyses, coupled with end-member mixing analysis derived from particle size measurements carried out on a ~3.3 m long core retrieved from Gayal el Bazal (southern Yemen) utilized to understand the late Holocene climatic fluctuations in the region. The current study shows that sediment accumulating in the lake comprises of allochthonous material (derived during pluvial events through surface runoff), precipitation of authigenic evaporite minerals (formed following changes in water composition and inflow strength during dry intervals), and aeolian activity (indicated by an increase in EM2 and calcite minerals). The multiproxy investigation displays enhanced precipitation during the MCA, marked by an increase in

detrital elements, higher TOC/TIC content, and dominance of EM1 (clayey silt fraction), which represent higher surface runoff in the lake watershed. Additionally, the higher contribution of EM2 (coarser silt fraction) appears to indicate aeolian input, coupled with increased gypsum production during the LIA, which indicate drier conditions. Our results show that the evolution of the Gayal el Bazal Lake has been mainly controlled by climatic factors (Solar and volcanic forcing), as the MCA and LIA are well imprinted in the sedimentary record. We further suggest that the Gayal el Bazal sedimentary archive has reliably responded to centennial-scale latitudinal variability of the ITCZ and associated with ISM. Comparison with other marine and terrestrial records from the Arabian Peninsula and Eastern Africa shows a similar climate pattern during the LIA and MCA intervals. We conclude that this work documents, for the first time, a continuous lacustrine record from southern Yemen that reliably responds to climate variability associated with the MCA and the LIA. Our work also proposes that the region's hydroclimate balance is sensitive to changes in solar activity, and thus if an extended solar minimum prevails in the future, it could affect the region, causing increased drought.

DATA AVAILABILITY STATEMENT

The original contributions presented in the study are included in the article/Supplementary Material, further inquiries can be directed to the corresponding author.

AUTHOR CONTRIBUTIONS

SP, JR, and NW designed the study. JR collected the samples, SP performed the measurements and carried out analysis on the samples, drafted the manuscript, and designed figures. NW and JR supervised the project made a substantial contribution to the concept or design of the article. All authors provided critical feedback and helped shape the research, analysis, and manuscript.

FUNDING

This research was supported by grants from PBC Fellowship program for International PhD students offered by the Council for Higher Education of Israel to SP.

ACKNOWLEDGMENTS

We are thankful to LacCore (National Lacustrine Core Facility), Department of Earth Sciences, University of Minnesota, for providing the sediments for the project. The authors acknowledge assistance with fieldwork from Douglas Schnurrenberger, who led fieldwork, and Prof. Juris Zarins. The American Institute for Yemeni Studies is thanked for their assistance with field logistics and project permitting. The authors warmly thanks Nimer Taha for assistance with grain size, XRD, and TOC/TIC measurements. This project was partially funded by Israel Science Foundation grant number 3413/21.

REFERENCES

Abbott, M. B., Seltzer, G. O., Kelts, K. R., and Southon, J. (1997). Holocene Paleohydrology of the Tropical Andes from lake Records. *Quat. Res.* 47 (1), 70–80. doi:10.1006/qres.1996.1874

Abu-Zied, R. H., and Bantan, R. A. (2015). Palaeoenvironment, Palaeoclimate and Sea-Level Changes in the Shuaiba Lagoon during the Late Holocene (Last 3.6 Ka), Eastern Red Sea Coast, Saudi Arabia. *The Holocene* 25 (8), 1301–1312. doi:10.1177/0959683615584204

Al-ameri, A., Schneider, M., Abu Lohom, N., and Sprenger, C. (2014). The Hydrogen (δD) and Oxygen (δ18 O) Isotopic Composition of Yemen's Rainwater. *Arab. J. Sci. Eng.* 39 (1), 423–436. doi:10.1007/s13369-013-0869-6

Al-Dousari, A. M., Al-Awadhi, J., and Ahmed, M. (2013). Dust Fallout Characteristics within Global Dust Storm Major Trajectories. *Arab J. Geosci.* 6 (10), 3877–3884. doi:10.1007/s12517-012-0644-0

Al-Dousari, A. M., and Al-Awadhi, J. (2012). Dust Fallout in Northern Kuwait, Major Sources and Characteristics. *Kuwait J. Sci.* 39 (2A), 171–187.

Almazroui, M. (2012). Dynamical Downscaling of Rainfall and Temperature over the Arabian Peninsula Using RegCM4. *Clim. Res.* 52, 49–62. doi:10.3354/cr01073

Anderson, D. M., Baulcomb, C. K., Duvivier, A. K., and Gupta, A. K. (2010). Indian Summer Monsoon during the Last Two Millennia. *J. Quat. Sci.* 25 (6), 911–917. doi:10.1002/jqs.1369

Andersson, R. A., Kuhry, P., Meyers, P., Zebühr, Y., Crill, P., and Mörth, M. (2011). Impacts of Paleohydrological Changes on N-Alkane Biomarker Compositions of a Holocene Peat Sequence in the Eastern European Russian Arctic. *Org. Geochem.* 42 (9), 1065–1075. doi:10.1016/j.orggeochem.2011.06.020

As-Saruri, M. A., and Wiefel, H. (2012). The Lithostratigraphic Subdivision of the Proterozoic Basement Rocks of the Mudiyah-Mukalla Area, Yemen. *Arab. J. Geosci.* 5 (5), 1127–1150. doi:10.1007/s12517-011-0295-6

Bakhlah, M. S., and Hassan, A. S. (2012). The Effect of Roof Colour on Indoor House Temperature in Case of Hadhramout, Yemen. *Am. Trans. Eng. Appl. Sci.* 1 (4), 2229–1652.

Bareille, G., Grousset, F. E., Labracherie, M., Labeyrie, L. D., and Petit, J.-R. (1994). Origin of Detrital Fluxes in the Southeast Indian Ocean during the Last Climatic Cycles. *Paleoceanography* 9 (6), 799–819. doi:10.1029/94pa01946

Baseer, M. N., Awad, A. M., and Almazroui, M. (2019). Climatology of the spring Red Sea Trough. *Int. J. Climatol.* 39 (11), 4218–4233. doi:10.1002/joc.6069

Berger, J.-F., Bravard, J.-P., Purdue, L., Benoist, A., Mouton, M., and Braemer, F. (2012). Rivers of the Hadramawt Watershed (Yemen) during the Holocene: Clues of Late Functioning. *Quat. Int.* 266, 142–161. doi:10.1016/j.quaint.2011.10.037

Berke, M. A., Johnson, T. C., Werne, J. P., Schouten, S., and Sinninghe Damsté, J. S. (2012). A Mid-holocene thermal Maximum at the End of the African Humid Period. *Earth Planet. Sci. Lett.* 351-352, 95–104. doi:10.1016/j.epsl.2012.07.008

Boës, X., Rydberg, J., Martinez-Cortizas, A., Bindler, R., and Renberg, I. (2011). Evaluation of Conservative Lithogenic Elements (Ti, Zr, Al, and Rb) to Study Anthropogenic Element Enrichments in lake Sediments. *J. Paleolimnol.* 46 (1), 75–87.

Boyle, J. F. (2005). "Inorganic Geochemical Methods in Palaeolimnology," in *Tracking Environmental Change Using Lake Sediments* (Springer Netherlands), 83–141.

Broccoli, A. J., Dahl, K. A., and Stouffer, R. J. (2006). Response of the ITCZ to Northern Hemisphere Cooling. *Geophys. Res. Lett.* 33 (1), L01702. doi:10.1029/2005gl024546

Broecker, W. S. (2001). Was the Medieval Warm Period Global. *Science* 291 (5508), 1497–1499. doi:10.1126/science.291.5508.1497

Bronk Ramsey, C. (2009). Bayesian Analysis of Radiocarbon Dates. *Radiocarbon* 51 (1), 337–360. doi:10.1017/s0033822200033865

Chawchai, S., Kylander, M. E., Chabangborn, A., Löwemark, L., and Wohlfarth, B. (2016). Testing Commonly Used X-ray Fluorescence Core Scanning-Based

Proxies for Organic-Rich lake Sediments and Peat. *Boreas* 45 (1), 180–189. doi:10.1111/bor.12145

Chen, F., Zhu, Y., Li, J., Shi, Q., Jin, L., and Wünemann, B. (2001). Abrupt Holocene Changes of the Asian Monsoon at Millennial- and Centennial-Scales: Evidence from lake Sediment Document in Minqin Basin, NW China. *Chin.Sci.Bull.* 46 (23), 1942–1947. doi:10.1007/bf02901902

Cronin, T. M., Hayo, K., Thunell, R. C., Dwyer, G. S., Saenger, C., and Willard, D. A. (2010). The Medieval Climate Anomaly and Little Ice Age in Chesapeake Bay and the North Atlantic Ocean. *Palaeogeogr. Palaeoclimatol. Palaeoecol.* 297 (2), 299–310. doi:10.1016/j.palaeo.2010.08.009

Croudace, I. W., Rindby, A., and Rothwell, R. G. (2006). ITRAX: Description and Evaluation of a New Multi-Function X-ray Core Scanner. *Geol. Soc. Lond. Spec. Publications* 267 (1), 51–63. doi:10.1144/gsl.sp.2006.267.01.04

Crouvi, O., Amit, R., Enzel, Y., Porat, N., and Sandler, A. (2008). Sand Dunes as a Major Proximal Dust Source for Late Pleistocene Loess in the Negev Desert, Israel. *Quat. Res.* 70 (2), 275–282. doi:10.1016/j.yqres.2008.04.011

Crowley, T. J., and Lowery, T. S. (2000). How Warm Was the Medieval Warm Period? *AMBIO: A J. Hum. Environ.* 29 (1), 51–54. doi:10.1579/0044-7447-29.1.51

Davies, C. P. (2006). Holocene Paleoclimates of Southern Arabia from Lacustrine Deposits of the Dhamar highlands, Yemen. *Quat. Res.* 66 (3), 454–464. doi:10.1016/j.yqres.2006.05.007

Davison, W. (1993). Iron and Manganese in Lakes. *Earth-Science Rev.* 34 (2), 119–163. doi:10.1016/0012-8252(93)90029-7

Dean, W. E., and Gorham, E. (1998). Magnitude and Significance of Carbon Burial in Lakes, Reservoirs, and Peatlands. *Geol* 26 (6), 535–538. doi:10.1130/0091-7613(1998)026<0535:masocb>2.3.co;2

Dessai, D. V. G., Nayak, G. N., and Basavaiah, N. (2009). Grain Size, Geochemistry, Magnetic Susceptibility: Proxies in Identifying Sources and Factors Controlling Distribution of Metals in a Tropical Estuary, India. *Estuarine, Coastal Shelf Sci.* 85 (2), 307–318. doi:10.1016/j.ecss.2009.08.020

Dietze, E., Hartmann, K., Diekmann, B., IJmker, J., Lehmkuhl, F., Opitz, S., et al. (2012). An End-Member Algorithm for Deciphering Modern Detrital Processes from lake Sediments of Lake Donggi Cona, NE Tibetan Plateau, China. *Sediment. Geology.* 243-244, 169–180. doi:10.1016/j.sedgeo.2011.09.014

Dietze, E., Wünnemann, B., Hartmann, K., Diekmann, B., Jin, H., Stauch, G., et al. (2013). Early to Mid-holocene lake High-Stand Sediments at Lake Donggi Cona, Northeastern Tibetan Plateau, China. *Quat. Res.* 79 (3), 325–336. doi:10.1016/j.yqres.2012.12.008

Edgell, H. (2006). *Arabian Deserts: Nature, Origin and Evolution*. Springer Science & Business Media.

Engstrom, D. R., and Wright, H. E., Jr (1984). "Chemical Stratigraphy of lake Sediments as a Record of Environmental Change," in *Lake Sediments and Environmental History: Studies in Palaeolimnology and Palaeoecology in Honour of Winifred Tutin*. Editors E. Y. Haworth and J. W. G. Lund (Leicester: Leicester University Press), 11.

Enzel, Y., Kushnir, Y., and Quade, J. (2015). The Middle Holocene Climatic Records from Arabia: Reassessing Lacustrine Environments, Shift of ITCZ in Arabian Sea, and Impacts of the Southwest Indian and African Monsoons. *Glob. Planet. Change* 129, 69–91. doi:10.1016/j.gloplacha.2015.03.004

Farquharson, F. A. K., Plinston, D. T., and Sutcliffe, J. V. (1996). Rainfall and Runoff in Yemen. *Hydrological Sci. J.* 41 (5), 797–811. doi:10.1080/02626669609491546

Fastook, J. L., Holmgren, K., Matthews, J. A., Odada, E., Karlén, W., Malmström, M., et al. (1999). Glacier Fluctuations on Mount Kenya since ~ 6000 Cal. Years BP: Implications for Holocene Climatic Change in Africa. *Stockholm* 28, 409–418.

Felis, T., Ionita, M., Rimbu, N., Lohmann, G., and Kölling, M. (2018). Mild and Arid Climate in the Eastern Sahara-Arabian Desert during the Late Little Ice Age. *Geophys. Res. Lett.* 45 (14), 7112–7119. doi:10.1029/2018gl078617

Feng, S., and Hu, Q. (2008). How the North Atlantic Multidecadal Oscillation May Have Influenced the Indian Summer Monsoon during the Past Two Millennia. *Geophys. Res. Lett.* 35 (1), L01707. doi:10.1029/2007gl032484

Fleitmann, D., Burns, S. J., Mangini, A., Mudelsee, M., Kramers, J., Villa, I., et al. (2007). Holocene ITCZ and Indian Monsoon Dynamics Recorded in Stalagmites from Oman and Yemen (Socotra). *Quat. Sci. Rev.* 26 (1-2), 170–188. doi:10.1016/j.quascirev.2006.04.012

Fleitmann, D., Burns, S. J., Neff, U., Mudelsee, M., Mangini, A., and Matter, A. (2004). Palaeoclimatic Interpretation of High-Resolution Oxygen Isotope Profiles Derived from Annually Laminated Speleothems from Southern Oman. *Quat. Sci. Rev.* 23 (7-8), 935–945. doi:10.1016/j.quascirev.2003.06.019

Fleitmann, D., Burns, S. J., Pekala, M., Mangini, A., Al-Subbary, A., Al-Aowah, M., et al. (2011). Holocene and Pleistocene Pluvial Periods in Yemen, Southern Arabia. *Quat. Sci. Rev.* 30 (7-8), 783–787. doi:10.1016/j.quascirev.2011.01.004

Fleitmann, D., and Matter, A. (2009). The Speleothem Record of Climate Variability in Southern Arabia. *Comptes Rendus Geosci.* 341 (8-9), 633–642. doi:10.1016/j.crte.2009.01.006

Gayo, E. M., Latorre, C., Santoro, C. M., Maldonado, A., and De Pol-Holz, R. (2012). Hydroclimate Variability in the Low-Elevation Atacama Desert over the Last 2500 Yr. *Clim. Past* 8 (1), 287–306. doi:10.5194/cp-8-287-2012

Graham, N. E., Ammann, C. M., Fleitmann, D., Cobb, K. M., and Luterbacher, J. (2011). Support for Global Climate Reorganization during the "Medieval Climate Anomaly. *Clim. Dyn.* 37 (5), 1217–1245. doi:10.1007/s00382-010-0914-z

Gupta, A. K., Anderson, D. M., and Overpeck, J. T. (2003). Abrupt Changes in the Asian Southwest Monsoon during the Holocene and Their Links to the North Atlantic Ocean. *Nature* 421 (6921), 354–357. doi:10.1038/nature01340

Gupta, A. K., Das, M., and Anderson, D. M. (2005). Solar Influence on the Indian Summer Monsoon during the Holocene. *Geophys. Res. Lett.* 32 (17), 1–4. doi:10.1029/2005gl022685

Hadden, R. L. (2012). *The Geology of Yemen: An Annotated Bibliography of Yemen's Geology, Geography and Earth Science*. Fort Belvoir, VA: Corps of Engineers Alexandria.

Håkanson, L., and Jansson, M. (1983). *Principles of lake Sedimentology*, 109. New Jersey: Blackburn Press, 24–31.

Hasanean, H., and Almazroui, M. (2015). Rainfall: Features and Variations over Saudi Arabia, a Review. *Climate* 3 (3), 578–626. doi:10.3390/cli3030578

Hehmeyer, I., Keall, E. J., and Rahimi, D. A. N. (2002). Ghayl Bā Wazīr: Applied Qanāt Technology in the Fissured Karst Landscape of Southern Yemen. *Proc. Semin. Arab. Stud.*, 32 83–97.

Hou, J., Tian, Q., Liang, J., Wang, M., and He, Y. (2017). Climatic Implications of Hydrologic Changes in Two lake Catchments on the central Tibetan Plateau since the Last Glacial. *J. Paleolimnol.* 58 (2), 257–273. doi:10.1007/s10933-017-9976-9

Hounslow, M. W., and Maher, B. A. (1999). Source of the Climate Signal Recorded by Magnetic Susceptibility Variations in Indian Ocean Sediments. *J. Geophys. Res.* 104 (B3), 5047–5061. doi:10.1029/1998jb900085

Ivakhnenko, O. P., Abirov, R., and Logvinenko, A. (2015). New Method for Characterisation of Petroleum Reservoir Fluidmineral Deposits Using Magnetic Analysis. *Energ. Proced.* 76, 454–462. doi:10.1016/j.egypro.2015.07.877

Jomelli, V., Lane, T., Favier, V., Masson-Delmotte, V., Swingedouw, D., Rinterknecht, V., et al. (2016). Paradoxical Cold Conditions during the Medieval Climate Anomaly in the Western Arctic. *Sci. Rep.* 6 (1), 32984–32989. doi:10.1038/srep32984

Khalaf, F., and Al-Hashash, M. (1983). Aeolian Sedimentation in the north-western Part of the Arabian Gulf. *J. Arid Environments* 6, 319–332. doi:10.1016/s0140-1963(18)31411-3

Kotlia, B. S., Ahmad, S. M., Zhao, J.-X., Raza, W., Collerson, K. D., Joshi, L. M., et al. (2012). Climatic Fluctuations during the LIA and post-LIA in the Kumaun Lesser Himalaya, India: Evidence from a 400 Y Old Stalagmite Record. *Quat. Int.* 263, 129–138. doi:10.1016/j.quaint.2012.01.025

Kuhnert, H., and Mulitza, S. (2011). Multi-decadal Variability and Late Medieval Cooling of Near-coastal Sea Surface Temperatures in the Eastern Tropical North Atlantic. *Paleoceanography* 26 (4), PA4224. doi:10.1029/2011pa002130

Kushnir, Y., and Stein, M. (2019). Medieval Climate in the Eastern Mediterranean: Instability and Evidence of Solar Forcing. *Atmosphere* 10 (1), 29. doi:10.3390/atmos10010029

Kylander, M. E., Ampel, L., Wohlfarth, B., and Veres, D. (2011). High-resolution X-ray Fluorescence Core Scanning Analysis of Les Echets (France) Sedimentary Sequence: New Insights from Chemical Proxies. *J. Quat. Sci.* 26 (1), 109–117. doi:10.1002/jqs.1438

Last, W. M. (2005). "Textural Analysis of Lake Sediments," in *Tracking Environmental Change Using Lake Sediments* (Springer), 41–81.

Lespez, L., Le Drezen, Y., Garnier, A., Rasse, M., Eichhorn, B., Ozainne, S., et al. (2011). High-resolution Fluvial Records of Holocene Environmental Changes in the Sahel: The Yamé River at Ounjougou (Mali, West Africa). *Quat. Sci. Rev.* 30 (5-6), 737–756. doi:10.1016/j.quascirev.2010.12.021

Levitus, S., Antonov, J. I., Wang, J., Delworth, T. L., Dixon, K. W., and Broccoli, A. J. (2001). Anthropogenic Warming of Earth's Climate System. *Science* 292 (5515), 267–270. doi:10.1126/science.1058154

Lézine, A. M., Robert, C., Cleuziou, S., Inizan, M. L., Braemer, F., Saliège, J. F., et al. (2010). Climate Change and Human Occupation in the Southern Arabian Lowlands during the Last Deglaciation and the Holocene. *Glob. Planet. Change* 72 (4), 412–428. doi:10.1016/j.gloplacha.2010.01.016

Lézine, A. M., Saliège, J. F., Robert, C., Wertz, F., and Inizan, M. L. (1998). Holocene Lakes from Ramlat As-Sab'atayn (Yemen) Illustrate the Impact of Monsoon Activity in Southern Arabia. *Quat. Res.* 50 (3), 290–299. doi:10.1006/qres.1998.1996

Lézine, A. M., Tiercelin, J. J., Robert, C., Saliège, J. F., Cleuziou, S., Inizan, M. L., et al. (2007). Centennial to Millennial-Scale Variability of the Indian Monsoon during the Early Holocene from a Sediment, Pollen and Isotope Record from the Desert of Yemen. *Palaeogeogr. Palaeoclimatol. Palaeoecol.* 243 (3-4), 235–249. doi:10.1016/j.palaeo.2006.05.019

Llasat, M. C., Llasat-Botija, M., Prat, M. A., Porcú, F., Price, C., Mugnai, A., et al. (2010). High-impact Floods and Flash Floods in Mediterranean Countries: The FLASH Preliminary Database. *Adv. Geosci.* 23, 47–55. doi:10.5194/adgeo-23-47-2010

Lou, J., Schwab, D. J., Beletsky, D., and Hawley, N. (2000). A Model of Sediment Resuspension and Transport Dynamics in Southern Lake Michigan. *J. Geophys. Res.* 105 (C3), 6591–6610. doi:10.1029/1999jc900325

Löwemark, L., Chen, H. F., Yang, T. N., Kylander, M., Yu, E. F., Hsu, Y. W., et al. (2011). Normalizing XRF-Scanner Data: A Cautionary Note on the Interpretation of High-Resolution Records from Organic-Rich Lakes. *J. Asian Earth Sci.* 40 (6), 1250–1256. doi:10.1016/j.jseaes.2010.06.002

Lüning, S., Gałka, M., Danladi, I. B., Adagunodo, T. A., and Vahrenholt, F. (2018). Hydroclimate in Africa during the Medieval Climate Anomaly. *Palaeogeogr. Palaeoclimatol. Palaeoecol.* 495, 309–322. doi:10.1016/j.palaeo.2018.01.025

Lüning, S., Gałka, M., and Vahrenholt, F. (2017). Warming and Cooling: The Medieval Climate Anomaly in Africa and Arabia. *Paleoceanography* 32 (11), 1219–1235. doi:10.1002/2017pa003237

Lüning, S., Schulte, L., Garcés-Pastor, S., Danladi, I. B., and Gałka, M. (2019). The Medieval Climate Anomaly in the Mediterranean Region. *Paleoceanogr. Paleoclimatology* 34 (10), 1625–1649. doi:10.1029/2019pa003734

Mann, M. E., Zhang, Z., Rutherford, S., Bradley, R. S., Hughes, M. K., Shindell, D., et al. (2009). Global Signatures and Dynamical Origins of the Little Ice Age and Medieval Climate Anomaly. *Science* 326 (5957), 1256–1260. doi:10.1126/science.1177303

Mardia, K. V., Kent, J. T., and Bibby, J. M. (1979). *Multivariate Analysis*, 15. London: Academic Press Inc. (London) Ltd, 518.

Marshall, W. A., Gehrels, W. R., Garnett, M. H., Freeman, S. P. H. T., Maden, C., and Xu, S. (2007). The Use of 'bomb Spike' Calibration and High-Precision AMS 14C Analyses to Date Salt-Marsh Sediments Deposited during the Past Three Centuries. *Quat. Res.* 68 (3), 325–337. doi:10.1016/j.yqres.2007.07.005

Matthews, J. A., and Briffa, K. R. (2005). The 'little Ice Age': Re-evaluation of an Evolving Concept. *Geografiska Annaler: Ser. A, Phys. Geogr.* 87 (1), 17–36. doi:10.1111/j.0435-3676.2005.00242.x

McLaren, P., and Bowles, D. (1985). The Effects of Sediment Transport on Grain-Size Distributions. *J. Sediment. Petrol.* 55 (4), 457–470. doi:10.1306/212f86fc-2b24-11d7-8648000102c1865d

Miller, G. H., Geirsdóttir, Á., Zhong, Y., Larsen, D. J., Otto-Bliesner, B. L., Holland, M. M., et al. (2012). Abrupt Onset of the Little Ice Age Triggered by Volcanism and Sustained by Sea-ice/ocean Feedbacks. *Geophys. Res. Lett.* 39 (2), L06605. doi:10.1029/2011gl050168

Miriyala, P., Sukumaran, N. P., Nath, B. N., Ramamurty, P. B., Sijinkumar, A. V., Vijayagopal, B., et al. (2017). Increased Chemical Weathering during the Deglacial to Mid-holocene Summer Monsoon Intensification. *Sci. Rep.* 7 (1), 44310–44311. doi:10.1038/srep44310

Mishra, P. K., Parth, S., Ankit, Y., Kumar, S., Ambili, V., Kumar, V. V., et al. (2019). Geochemical and Sedimentological Characteristics of Surface Sediments from Ashtamudi Estuary, Southern India: Implications for Provenance and Modern Sedimentary Dynamics. *Environ. Earth Sci.* 78 (14), 1–11. doi:10.1007/s12665-019-8376-z

Mueller, A. D., Islebe, G. A., Hillesheim, M. B., Grzesik, D. A., Anselmetti, F. S., Ariztegui, D., et al. (2009). Climate Drying and Associated forest Decline in the Lowlands of Northern Guatemala during the Late Holocene. *Quat. Res.* 71 (2), 133–141. doi:10.1016/j.yqres.2008.10.002

Murray, M. R. (2002). Is Laser Particle Size Determination Possible for Carbonate-Rich lake Sediments. *J. Paleolimnol.* 27 (2), 173–183. doi:10.1023/a:1014281412035

Neugebauer, I., Schwab, M. J., Waldmann, N. D., Tjallingii, R., Frank, U., Hadzhiivanova, E., et al. (2016). Hydroclimatic Variability in the Levant during the Early Last Glacial (~ 117-75 Ka) Derived from Micro-facies Analyses of Deep Dead Sea Sediments. *Clim. Past* 12 (1), 75–90. doi:10.5194/cp-12-75-2016

Neukom, R., Steiger, N., Gómez-Navarro, J. J., Wang, J., and Werner, J. P. (2019). No Evidence for Globally Coherent Warm and Cold Periods over the Preindustrial Common Era. *Nature* 571 (7766), 550–554. doi:10.1038/s41586-019-1401-2

Otto-Bliesner, B. L., Brady, E. C., Fasullo, J., Jahn, A., Landrum, L., Stevenson, S., et al. (2016). Climate Variability and Change since 850 CE: An Ensemble Approach with the Community Earth System Model. *Bull. Am. Meteorol. Soc.* 97 (5), 735–754. doi:10.1175/bams-d-14-00233.1

Peinerud, E. K. (2000). Interpretation of Si Concentrations in lake Sediments: Three Case Studies. *Environ. Geology.* 40 (1-2), 64–72. doi:10.1007/pl00013330

Philippsen, B. (2013). The Freshwater Reservoir Effect in Radiocarbon Dating. *Heritage Sci.* 1 (1), 1–19. doi:10.1186/2050-7445-1-24

Pleskot, K., Tjallingii, R., Makohonienko, M., Nowaczyk, N., and Szczuciński, W. (2018). Holocene Paleohydrological Reconstruction of Lake Strzeszyńskie (Western Poland) and its Implications for the central European Climatic Transition Zone. *J. Paleolimnol* 59 (4), 443–459. doi:10.1007/s10933-017-9999-2

Pollastro, R. M., Karshbaum, A. S., and Viger, R. J. (1999). *Open-File Report 97-470B Maps Showing Geology, Oil and Gas fields and Geologic Provinces of the Arabian Peninsula*. Reston, VA: US Geological Survey.

Ramsey, C. B. (2008). Deposition Models for Chronological Records. *Quat. Sci. Rev.* 27 (1-2), 42–60. doi:10.1016/j.quascirev.2007.01.019

Rawat, V., Rawat, S., Srivastava, P., Negi, P. S., Prakasam, M., and Kotlia, B. S. (2021). Middle Holocene Indian Summer Monsoon Variability and its Impact on Cultural Changes in the Indian Subcontinent. *Quat. Sci. Rev.* 255, 106825. doi:10.1016/j.quascirev.2021.106825

Reimer, P. J., Austin, W. E. N., Bard, E., Bayliss, A., Blackwell, P. G., Bronk Ramsey, C., et al. (2020). The IntCal20 Northern Hemisphere Radiocarbon Age Calibration Curve (0-55 Cal kBP). *Radiocarbon* 62 (4), 725–757. doi:10.1017/rdc.2020.41

Rodwell, M. J., and Hoskins, B. J. (1996). Monsoons and the Dynamics of Deserts. *Q.J R. Met. Soc.* 122, 1385–1404. doi:10.1002/qj.49712253408

Rothwell, R. G. (2015). "Twenty Years of XRF Core Scanning Marine Sediments: What Do Geochemical Proxies Tell Us," in *Micro-XRF Studies Of Sediment Cores* (Dordrecht: Springer), 25–102.

Ruddiman, W. F. (2013). The Anthropocene. *Annu. Rev. Earth Planet. Sci.* 41, 45–68. doi:10.1146/annurev-earth-050212-123944

Schettler, G., Liu, Q., Mingram, J., Negendank, J. F. W., and Negendank, F. W. (2006). Palaeovariations in the East-Asian Monsoon Regime Geochemically Recorded in Varved Sediments of Lake Sihailongwan (Northeast China, Jilin Province). Part 1: Hydrological Conditions and Dust Flux. *J. Paleolimnol* 35 (2), 239–270. doi:10.1007/s10933-005-0096-6

Schneider, T., Bischoff, T., and Haug, G. H. (2014). Migrations and Dynamics of the Intertropical Convergence Zone. *Nature* 513 (7516), 45–53. doi:10.1038/nature13636

Schnurrenberger, D., Russell, J., and Kelts, K. (2003). Classification of Lacustrine Sediments Based on Sedimentary Components. *J. Paleolimnol.* 29 (2), 141–154. doi:10.1023/a:1023270324800

Shakun, J. D., Burns, S. J., Fleitmann, D., Kramers, J., Matter, A., and Al-Subary, A. (2007). A High-Resolution, Absolute-Dated Deglacial Speleothem Record of Indian Ocean Climate from Socotra Island, Yemen. *Earth Planet. Sci. Lett.* 259 (3-4), 442–456. doi:10.1016/j.epsl.2007.05.004

Shindell, D. T., Schmidt, G. A., Mann, M. E., Rind, D., and Waple, A. (2001). Solar Forcing of Regional Climate Change during the Maunder Minimum. *Science* 294 (5549), 2149–2152. doi:10.1126/science.1064363

Singhvi, A. K., and Kar, A. (2004). The Aeolian Sedimentation Record of the Thar Desert. *J. Earth Syst. Sci.* 113 (3), 371–401. doi:10.1007/bf02716733

Sinha, R., Smykatz-Kloss, W., Stüben, D., Harrison, S. P., Berner, Z., and Kramar, U. (2006). Late Quaternary Palaeoclimatic Reconstruction from the Lacustrine Sediments of the Sambhar Playa Core, Thar Desert Margin, India. *Palaeogeogr. Palaeoclimatol. Palaeoecol.* 233 (3-4), 252–270. doi:10.1016/j.palaeo.2005.09.012

Sly, P. G. (1994).*Sedimentary Processes in Lakes* in *Lakes* (Springer), 65–89.

Solohub, J. T., and Klovan, J. E. (1970). Evaluation of Grain-Size Parameters in Lacustrine Environments. *J. Sediment. Res.* 40 (1), 81–101. doi:10.1306/74d71efb-2b21-11d7-8648000102c1865d

Staubwasser, M., Sirocko, F., Grootes, P. M., and Erlenkeuser, H. (2002). South Asian Monsoon Climate Change and Radiocarbon in the Arabian Sea during Early and Middle Holocene. *Paleoceanography* 17 (4), 15–12. doi:10.1029/2000pa000608

Steinhilber, F., Abreu, J. A., Beer, J., Brunner, I., Christl, M., Fischer, H., et al. (2012). 9,400 Years of Cosmic Radiation and Solar Activity from Ice Cores and Tree Rings. *Proc. Natl. Acad. Sci.* 109 (16), 5967–5971. doi:10.1073/pnas.1118965109

Stuut, J. B. W., Prins, M. A., Schneider, R. R., Weltje, G. J., Fred Jansen, J. H., and Postma, G. (2002). A 300-kyr Record of Aridity and Wind Strength in Southwestern Africa: Inferences from Grain-Size Distributions of Sediments on Walvis Ridge, SE Atlantic. *Mar. Geol.* 180 (1-4), 221–233. doi:10.1016/s0025-3227(01)00215-8

Sun, D., Bloemendal, J., Rea, D. K., Vandenberghe, J., Jiang, F., An, Z., et al. (2002). Grain-size Distribution Function of Polymodal Sediments in Hydraulic and Aeolian Environments, and Numerical Partitioning of the Sedimentary Components. *Sediment. Geol.* 152 (3-4), 263–277. doi:10.1016/s0037-0738(02)00082-9

Thompson, R., and Morton, D. J. (1979). Magnetic Susceptibility and Particle-Size Distribution in Recent Sediments of the Loch Lomond Drainage basin, Scotland. *J. Sediment. Res.* 49 (3), 801–811. doi:10.1306/212f7851-2b24-11d7-8648000102c1865d

Tierney, J. E., Ummenhofer, C. C., and Demenocal, P. B. (2015). Past and Future Rainfall in the Horn of Africa. *Sci. Adv.* 1 (9), e1500682. doi:10.1126/sciadv.1500682

Tierney, J. E., Russell, J. M., Damsté, J. S. S., Huang, Y., and Verschuren, D. (2011). Late Quaternary Behavior of the East African Monsoon and the Importance of the Congo Air Boundary. *Quat. Sci. Rev.* 30 (7-8), 798–807. doi:10.1016/j.quascirev.2011.01.017

Toker, E., Sivan, D., Stern, E., Shirman, B., Tsimplis, M., and Spada, G. (2012). Evidence for Centennial Scale Sea Level Variability during the Medieval Climate Optimum (Crusader Period) in Israel, Eastern Mediterranean. *Earth Planet. Sci. Lett.* 315-316, 51–61. doi:10.1016/j.epsl.2011.07.019

Trenberth, K. E., Dai, A., Rasmussen, R. M., and Parsons, D. B. (2003). The Changing Character of Precipitation. *Bull. Am. Meteorol. Soc.* 84 (9), 1205–1218. doi:10.1175/bams-84-9-1205

Vaasma, T. (2008). Grain-size Analysis of Lacustrine Sediments: a Comparison of Pre-treatment Methods. *Estonian J. Ecol.* 57 (4), 231–243. doi:10.3176/eco.2008.4.01

Van Rampelbergh, M., Fleitmann, D., Verheyden, S., Cheng, H., Edwards, L., De Geest, P., et al. (2013). Mid- to Late Holocene Indian Ocean Monsoon Variability Recorded in Four Speleothems from Socotra Island, Yemen. *Quat. Sci. Rev.* 65, 129–142. doi:10.1016/j.quascirev.2013.01.016

Vandenberghe, J. (2013). Grain Size of fine-grained Windblown Sediment: A Powerful Proxy for Process Identification. *Earth-Science Rev.* 121, 18–30. doi:10.1016/j.earscirev.2013.03.001

Venables, W. N., and Ripley, B. D. (2002). *Exploratory Multivariate Analysis*. New York, NY): Springer, 301–330. doi:10.1007/978-0-387-21706-2_11

Warner, T. (2009). *Desert Meteorology*. Cambridge: Cambridge University Press.

Wassenburg, J. A., Dietrich, S., Fietzke, J., Fohlmeister, J., Jochum, K. P., Scholz, D., et al. (2016). Reorganization of the North Atlantic Oscillation during Early Holocene Deglaciation. *Nat. Geosci* 9 (8), 602–605. doi:10.1038/ngeo2767

Weltje, G. J. (1997). End-member Modeling of Compositional Data: Numerical-Statistical Algorithms for Solving the Explicit Mixing Problem. *Math. Geol.* 29 (4), 503–549. doi:10.1007/bf02775085

Weltje, G. J., and Tjallingii, R. (2008). Calibration of XRF Core Scanners for Quantitative Geochemical Logging of Sediment Cores: Theory and Application. *Earth Planet. Sci. Lett.* 274 (3-4), 423–438. doi:10.1016/j.epsl.2008.07.054

WorldClim (2021). Available at: https://worldclim.org/(Accessed March 17, 2021).

Wünnemann, B., Demske, D., Tarasov, P., Kotlia, B. S., Reinhardt, C., Bloemendal, J., et al. (2010). Hydrological Evolution during the Last 15 Kyr in the Tso Kar lake basin (Ladakh, India), Derived from Geomorphological, Sedimentological and Palynological Records. *Quat. Sci. Rev.* 29 (9-10), 1138–1155. doi:10.1016/j.quascirev.2010.02.017

Xu, H., Hou, Z. H., Ai, L., and Tan, L. C. (2007). Precipitation at Lake Qinghai, NE Qinghai–Tibet Plateau, and its Relation to Asian Summer Monsoons on Decadal/interdecadal Scales during the Past 500 Years. *Palaeogeogr. Palaeoclimatol. Palaeoecol.* 254 (3-4), 541–549. doi:10.1016/j.palaeo.2007.07.007

Xue, J., Lee, C., Wakeham, S. G., and Armstrong, R. A. (2011). Using Principal Components Analysis (PCA) with Cluster Analysis to Study the Organic Geochemistry of Sinking Particles in the Ocean. *Org. Geochem.* 42 (4), 356–367. doi:10.1016/j.orggeochem.2011.01.012

Yanhong, Y., Andreas, L., Bernd, W., Li, S., and Wang, S. (2007). Holocene Climate Change in the Central Tibetan Plateau Inferred by Lacustrine Sediment Geochemical Records. *Sci. China Ser. D: Earth Sci.* 50 (10), 1548–1555. doi:10.1007/s11430-007-0113-x

Zhao, C., Yu, Z., Zhao, Y., Ito, E., Kodama, K. P., and Chen, F. (2010). Holocene millennial-scale climate variations documented by multiple lake-level proxies in sediment cores from Hurleg Lake, Northwest China. *J Paleolimnol* 44 (4), 995–1008. doi:10.1007/s10933-010-9469-6

Zolitschka, B., Mingram, J., Van Der Gaast, S., Jansen, J. F., and Naumann, R. (2002). *Sediment Logging Technique in Tracking Environmental Change Using lake Sediments*. Dordrecht: Springer, 137–153.

Conflict of Interest: The authors declare that the research was conducted in the absence of any commercial or financial relationships that could be construed as a potential conflict of interest.